

POLITECNICO DI TORINO

SCUOLA DI DOTTORATO

Dottorato in Ingegneria Elettronica
e delle Comunicazioni – XXV ciclo

Tesi di Dottorato

**Numerical simulation and
design of semiconductor
quantum dot-based
lasers and amplifiers**



Tianhong Xu

matr. 169428

Tutore

Prof. Ivo Montrosset

Coordinatore del corso di dottorato

Prof. Ivo Montrosset

January 2013

Abstract

The development in the manufacture of high quality self-assembled quantum dot materials, as well as their superior properties with respect to the bulk and quantum well counterparts, has inspired in the last 10 years intensive realization and investigation activities carried on the quantum dot-based devices. In this thesis we focus on the theoretical analysis and design of two main classes of optical devices based on the InAs/In_{0.15}Ga_{0.85}As quantum dots active medium: the two-section passively mode-locked quantum dot lasers and the tapered semiconductor optical amplifiers. These activities have been performed within the Seventh Framework European Project "Fast Dot", aiming to achieve high-power ultra-fast laser sources. In the project, fruitful collaborations within different partners have been established.

In the first main subject of this thesis, two numerical models are introduced, which with respect to the models available in the literature, are capable to simulate particular mode-locked lasers where simultaneous ground state and excited state pulses with different group velocities exist. These models therefore show more flexibility when simulating quantum dot mode-locked lasers.

Passively mode-locked quantum dot lasers generating picosecond or sub-picosecond optical pulses for applications ranging from telecommunication to medicine have been comprehensively analyzed via the above-mentioned models. The complex physical mechanisms that exist in such devices and are detrimental for the pulse formation were studied. Based on these studies, efforts were devoted to search for the possibility to optimise the output performances of a mode-locked laser by changing both the device geometry and the active material. Our simulation results show good qualitative agreement with the experimental findings and give therefore reliable design guidance of the passively ML lasers. Finally, we present a systematic investigation of a particular regime where simultaneous mode-locking pulses from the fundamental ground state and the excited state transitions in the quantum dots are achieved. Pulses with extremely enhanced peak power, pulse width and stability were observed in this dual-state mode-locking regime.

The second main subject of this thesis is the design and analysis of tapered semiconductor optical amplifiers operating at high power regime. We developed a numerical model that allows reliable description of the optical

field propagation in an axially varying waveguide. Additionally, by combining the beam propagation equation with pre-calculated results obtained from the multi-population rate-equation system, we could model rigorously and efficiently the non-linear gain and refractive index variation occurring in the quantum dot active medium at high power regime. This model is then extensively applied to the simulation of the gain-guided and weakly index guided tapered semiconductor optical amplifiers in collaboration with the project partners that carried out the device fabrication and characterization. Our simulations contributed to design the high performance semiconductor optical amplifiers used in the master-oscillator power-amplifier structure for the amplification of a stream of high power pulses.

Finally, we show two additional usages of above beam propagation method model in the design of electro-optic devices: the first one is to study the anti-reflection ability of a tapered waveguide with tilted end facet; the second one is to simulate the axially varying lasers in continuous wave regime, and from which parameters describing the field propagation along the non-uniform waveguide can be extracted and used as an input to the finite-difference time-domain or multi-section delayed differential equation model for the dynamic simulation of lasers with the same geometry but working in the ML regime.

Acknowledgements

” There is no royal road to science, and only those who do not dread the fatiguing tomb of its steep paths have a chance of gaining its luminous summits”. Fortunately, I never felt lonely or helpless during my journey on the road of science in past three years. There were guides when I was confused; there were supports when I was tired; there were also people for sharing when I was happy. Now, this is almost the end of my graduate study, but this is also a new beginning in my life, full with hopes and possibilities. Therefore, I want to take this chance to express my sincere acknowledgement to many people for their selfless helps to me.

I have to thank my parents, not only because they are the first teachers in my life, but also because they do their best, even self-sacrifice, to let me grow up with happiness, healthy and self-confidence. Particular thanks should also be send to my husband, for always being with me for encouraging and supporting.

Deepest gratitude to my supervisor, Prof. Montrosset, for leading me into this interesting and exciting field of photonics, for his constant guidances and supports in every stage of my learning road on this field, for the opportunity he gives me to join and collaborate with many researchers all around Europe and for his patient help and impressive kindness when I met problems in the study or in the life.

I want to extend my special thanks to Mattia Rossetti and Paolo Bardella for all the clear and patient introductions they giving to me at the very beginning of my Ph.D journey, for all the extremely useful collaborations and discussions between us in previous years, for all their interesting introductions of Italy and Italian and finally for all their warm-hearted helps and concerns.

Many thanks to Mariangela Gioannini, who is also the first guide for teaching me about how to do the modeling and simulation of the optical semiconductor devices when I was preparing my Master degree thesis. I am heavily indebted to her for her tolerance to my stupid mistakes and questions at that period, for her patient correctness of them and for her fruitful collaborations in my Ph.D period.

I would like to thank also the friends I met in this group during these three years, Marco Vallone, Aariel Cedola and Marcelo Cappelletti for the

interesting conversations on various directions. Especially, I real enjoy the pleasant atmosphere and the passion brought from Argentine to this group by Aariel and Marcelo.

Last but not least, the particular acknowledgement must be sent to the Professors and researchers I was collaborated with in the framework of the "FastDot" EU project. Many of our simulations and findings would never have been achieved without their experimental results, experiences, comments and helps. Among the others, Maria Ana Cataluna, Daniil Nikitichev and Ying Ding at the University of Dundee (UK); Charis Mesaritakis, Alexandros Kapsalis and Dimitris Syvridis at the National and Kapodistrian from University of Athens, NKUA (Greece); Michel Krakowski and coworkers at the III-V Lab Alcatel-Thales (France); Lukas Drzewietzki and Prof. Wolfgang Elsäßer at the Technische Universität Darmstadt (Germany); Igor krestnikov and coworkers at Innolume GmbH (Germany).

Contents

Abstract	i
Acknowledgements	iii
1 Introduction	1
1.1 Motivation: advantages of QD-based devices	1
1.2 QD: fabrication and related properties	4
1.3 QD edge emitting devices	7
1.4 Thesis outline	12
2 QD-based dual-state laser modeling	14
2.1 Electromagnetic field dynamics	15
2.2 Carrier dynamics in the active medium	18
2.2.1 Rate equation system for the current injection section	20
2.2.2 Rate equation system for the reverse biased section . .	24
2.3 Optical response of the active medium	27
2.3.1 Polarisation induced by an electromagnetic field . . .	27
2.3.2 Spontaneous emission noise	30
2.4 Single-population dual-state FDTW model	30
2.5 Multi-section dual-state DDE model	36
2.6 Conclusion	42
3 Passively mode locked QD lasers	43
3.1 Introduction of passive ML	45
3.2 Special advantages of QD ML lasers	53
3.3 GS ML performances improvement	56
3.3.1 Lasers with higher value of the stability parameter S .	57
3.3.2 Lasers with the same value of the stability parameter S	67
3.4 Relation between the intracavity pulse evolution and the ML	
performances	71
3.4.1 Investigation approach and the considered devices . .	72
3.4.2 Investigation and discussion	73
3.5 Dual-state ML regime	82
3.5.1 Gain and absorption dynamics	84

3.5.2	Sole GS ML and dual-state ML	90
3.5.3	Sole ES ML	99
3.6	Conclusion	100
4	CW longitudinally-varying QD devices	102
4.1	Numerical modeling via FD-BPM	103
4.2	Investigation of tapered SOA	110
4.2.1	General properties and design strategies	110
4.2.2	Simulation of a typical tapered SOA	112
4.2.3	Performances improvement for tapered SOA	115
4.3	Study of end facet back-reflection	117
4.4	Study of tapered QD-based laser	120
4.5	Conclusion	124
5	Conclusions and future works	125
	References	127
	Journal publications	138

Chapter 1

Introduction

Before introducing my work during these three years, in this chapter, main properties of the semiconductor quantum dot (QD) based devices and the related underlying physical mechanisms which are essential to understand following content are briefly reviewed. Detailed introduction and explanation of these properties should refer to other literatures or specific books.

The chapter begins by outlining the motivation for exploiting semiconductor QD material in the design of lasers or optical amplifiers. Desirable effects and characteristics of this three dimensional (3D) quantum confined material are described, showing QDs medium as a superior alternative to the traditional bulk and quantum well (QW) groups. Then in Section 1.2, fabrication method of QDs are recalled phenomenologically together with the associated key properties of the QDs resulting from this kind of fabrication approach, such as the inhomogeneous broadening of the QD ensembles and consequently the inhomogeneous broadening in the gain spectrum. The transversal direction epitaxial structure and the lateral direction patterning of the active region for QD-based device investigated in this thesis are presented in Section 1.3. Finally, structure of the whole thesis is outlined.

1.1 Motivation: characteristics and advantages of QD-based devices

Semiconductor laser diode (LD) represents one main class of lasers so far. Comparing to its competitors, the gas laser and the solid-state laser, semiconductor LD owns many well known distinguishing advantages, such as easy manufacturability, compactness, high potential for integration, direct electrical pumping, low power consumption and high reliability (useful lifetime) etc. As a result, it has been proposed as promising candidate in a large number of electro-optic applications and has already been widely used.

The first semiconductor laser was demonstrated in 1962 [1], since then,

great efforts have been done to improve the performances of the LDs, including developments both in the laser waveguide structures and the semiconductor materials, such as the distributed Bragg reflector laser (DBR) [2], the distributed feedback laser (DFB) [3] and the double heterostructure (DH) laser [4]. Among the others, Dingle and Henry demonstrated the QW laser in 1974 [5]. In this device, the carriers are confined within the quantized energy levels contributing to large reduction of the threshold current density and enabling the control of the lasing wavelength by simply changing the thickness of the QW layer. This modification in the electronic band structure using the quantum confinement along one spatial dimension resulted in various new optical and electronic properties. As a matter of fact, developments of QW LDs during last 30 years led to revolutionary changes in the characters and performances of these devices. With these achievements, it is very nature to expect that higher order quantization of the band structure should allow even better qualities with respect to that of the QW medium. Although it is difficult to realize additional degrees of quantization, continuous improvement in the epitaxial growth technology has made these theoretical derivations coming true. Quantum wire representing carrier confinement in two dimensions (2D) and quantum dot representing the full three-dimensional confinement of the carriers have been demonstrated one by one.

Since the electrons are confined in a small space with nanometer scale along all the three spatial dimensions, zero-dimensional electronic potential well is formed in QD, which indicates that the number of dimensions in which electron can act as a free carrier is zero in this case. Under this condition, QD electronic structure is characterized by a set of discrete energy levels very similar to those obtained in a single atom. Therefore, QDs are also referred as artificial atoms. This special electronic band structure represents the fundamental difference between a QD active medium and a QW or a bulk active medium.

As schematically shown in Fig. 1.1a, the density of state of a bulk medium has a parabolic shape. In principle, the density of carriers $n(E)$ in a semiconductor is calculated as the product of the density of states $N(E)$ and the occupation probability of that state $f(E)$ being E the state energy (see Fig. 1.1a). Moreover, the emission spectrum of this material relates directly to its carrier density profile. Unfortunately, in real bulk semiconductors, both the peak density and the width of the distribution for $n(E)$ will change if the operation condition is changed, such as temperature or external excitation. These changes lead to corresponding variations in the emission spectrum of this material and consequently undesired variations in the performances. On the contrary, the density of states for one QD has a Dirac delta function distribution, which is, although broadened somewhat at practical temperature, much narrower than bulk materials. Additionally, the energy separation between different discrete states is large enough to

result in significant changes in the occupation probability and consequently in the carrier density for different states (see Fig. 1.1b).

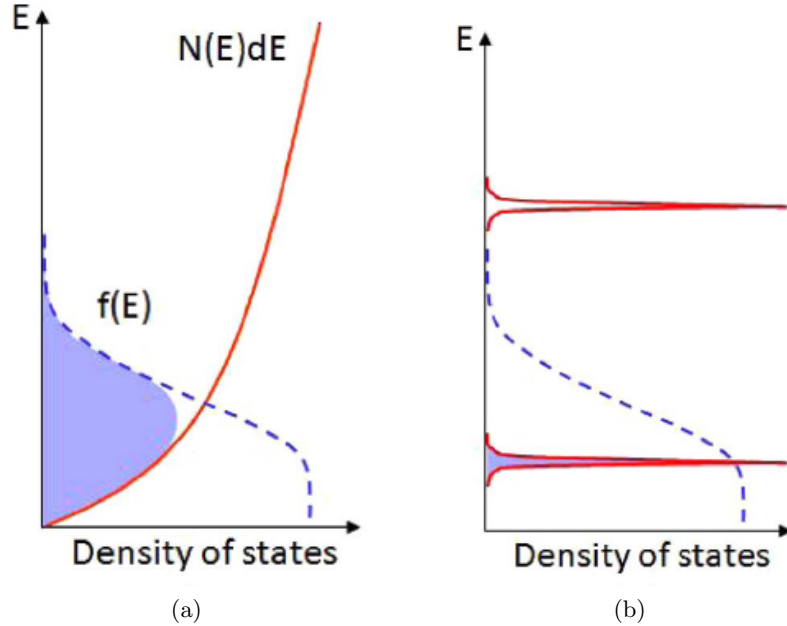


Figure 1.1: (a) Density of states, Fermi function and density of carriers for a bulk semiconductor. (b) Dirac delta function density of states for QD material (from reference [6]).

Due to the atom-like energy levels and the delta-function-like density of states, QD materials were expected to show significant operational advantages in many aspects. Since the position of the state energy is almost immune to the operation condition changes, emission wavelength of this material is stabilized. Furthermore, as the energy separation between discrete states is larger than the thermal energy $k_B T$, variation of Fermi level around the lowest state results in little to no changes in the carrier density, consequently a almost temperature independent threshold current can be achieved. Then as been show in Fig. 1.1b, due to smaller density of states, QD material requires fewer injected carriers to achieve population inversion, leading therefore to a reduction in the threshold current density and an increase in the differential gain/absorption. Besides, due to the Dirac delta shape of emission spectrum, a zero linewidth enhancement factor in QD-based devices are expected [7]. However, these potential advantages hold just to a certain extent in the real QD lasers.

The Stranski-Krastanov growth mechanism is commonly used to generate QD ensembles [8], which are the so-called self-assembled quantum dots. Due to the inherent property of this growth mechanism, large dispersion in terms of size and composition usually happens in the generated QD en-

sembles. As an evidence, inhomogeneous broadening of the gain spectrum has been observed in the QD devices and the full-width at half-maximum (FWHM) of the gain spectrum in the range of 20 - 42 meV has been reported [9, 10, 11]. Moreover, such statistic dispersion in QD ensembles and the inhomogeneous broadening of the gain spectrum also cause a reduction in the maximum achievable material gain and a non-zero linewidth enhancement factor in QD-based devices.

So far, the best reported characteristics for QD lasers correspond to the ordinary *O*-band telecommunication window around 1300 nm. This wavelength is also the operating wavelength for devices considered in this thesis. Although above mentioned degradation effects exist, extraordinary performances, including low threshold current of 17 A/cm² [12], high temperature insensitivity [13], near-zero linewidth enhancement factor [14], large differential gain [15] and relatively large small signal bandwidth of 12 GHz [16] have been reported for QD-based light sources emitting around 1.3 μ m.

To conclude, the novel generation of optoelectronic devices based on QD active media, such as the edge-emitting lasers and the semiconductor optical amplifiers (SOA), contains a large range of advantages with respect to the conventional bulk and QW counterparts, and show therefore high potential in various applications, including future all-optical signal processing, telecommunication, material processing, metrology and medicine.

Since both the optical material and the device structure are becoming more and more complicated, conventional simple analytic model can not supply sufficient description of the underlying physical mechanisms in such kind of devices any more, therefore limiting their usage in the purpose of device performance prediction and device design guidance. Under this condition, sophisticated numerical models emerge their effectiveness and reliability as a means to get the fundamental understanding of advanced photonic structures and in turn to develop new photonic devices. For this purpose in following chapters several numerical models, with different levels of complexity and different functionalities are introduced and employed for analysis of QD-based devices. In advance, the optical and electronic structures of such devices, which are essential information to develop the numerical model, will be shown in Section 1.2 and Section 1.3.

1.2 Introduction of QD: fabrication and related physical properties

Thanks to the significant progresses in the epitaxial processes such as Molecular Beam Epitaxy (MBE) and Metal Organic Chemical Vapour Deposition (MOCVD), atom-like QD optical medium has been realized [17]. Self-assembled QDs grown by MBE exploiting the Stranski-Krastanov (SK) growth mechanism [8] represent the main class of QD materials so far with

characteristic emission wavelengths ranging from $1 \mu m$ to $1.8 \mu m$. The attraction of the self-assembly process for laser diodes is that it employs standard semiconductor growth processes to deposit layers of dots within the slab waveguide and the p-n junction structure of a standard diode laser.

Traditionally, MBE has been used for decades to grow semiconductor thin layers for multiple layer heterostructure. This technique is essentially used for the growth of lattice-matched, or nearly lattice-matched, epitaxial layers on a suitable single crystal substrate. During the growing process, an entire atomic layer of material is deposited before the growth of the next atomic layer and the generation of undesirable dislocations of new arriving atoms should be kept to a minimum. Generally, this layer-by-layer growth is characterized by lattice-matched systems or lightly strained systems below a critical thickness. Therefore, the result of this growth is a conformal single uniform layer of material as shown in Fig. 1.2a.

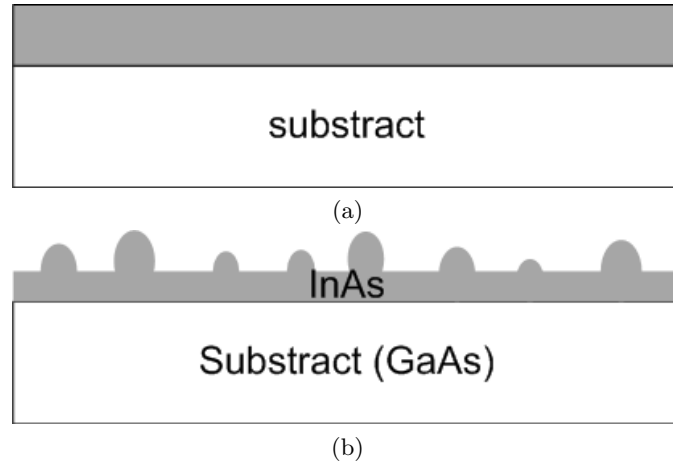


Figure 1.2: Cross-section view of (a) traditional uniform epitaxial layer growth and (b) self-assembled QDs growth based on SK process.

On the contrary, if the difference between the lattice constant (a) of the grown material and the substrate exceeds a certain critical value, for example InAs on the GaAs substrate ($\Delta a/a = 7\%$), big strain energy generates during the layer growth. In this Stranski-Krastanov growth, initially the lattice parameter of the InAs layer tends to match that of the GaAs substrate; strain energy generated in this layer is not large enough now, thus forming a thin strained 2D layer. After some number of atomic layers is deposited (typically 1-2 monolayers), sufficient strain energy has accumulated that conventional 2D epitaxial layer is unfavorable and the growth transits from layer to island, as shown in Fig. 1.2b. The initially thin 2D layer is usually called as the wetting-layer (WL).

Above mechanism is the basis for generating the self-assembled quantum dots (see complete review in [18] and [19]). A big advantage of it for

the optoelectronic applications is that the phase transition from the epitaxial layer to the random arrangement of QDs relieves the strain elastically without introducing defects or recombination centres.

As mentioned in Section 1.1, this natural process of the QD islands formation implies a statistical distribution of all the QD properties, such as size, shape and material composition (see Fig. 1.3). Typically, QDs produced by the SK mechanism have pyramidal or lens shapes with characteristic diameter in the range of 25 nm, height of 3-5 nm and a surface density of $1-10 \cdot 10^{10} \text{ cm}^{-2}$ [19]. In addition, the thickness of the wetting layer can be 3-4 nm [20] [21].

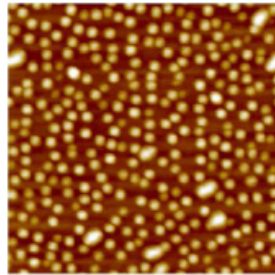


Figure 1.3: $500 \times 500 \text{ nm}^2$ AFM image of self-assembled InAs QDs grown on the (100) oriented GaAs substrate (from reference [18]).

As a matter of fact, the size, the shape and the material composition of the QDs determine the electronic potential profile and consequently the energy level scheme for a particular QD. Changing these properties throughout the QD ensembles, the energy of the optically active interband transitions will be significantly modified from dot to dot.

Ideally, identical dots are expected to have the same energy level scheme and therefore have a sharp spectral gain profile characterized by a Lorentzian function which is homogeneous broadened and the linewidth of it varies with the carrier density and the temperature. A schematic of such Lorentzian-shape gain spectrum is shown in Fig. 1.4a. Since the self-assembled QDs are unlikely to be identical in size and shape, the electronic states will be different in energy due to the strong dependence of the 3D quantum confinement on the dot size variation. Therefore, the overall gain spectrum from the QD ensembles is essentially an independent sum of all the individual components. This leads to a significant inhomogeneous broadening in the spectrum profile with characteristic FWHM linewidth in the range of 20-42 meV, as shown in Fig. 1.4b.

A rigorous numerical modeling of above described QD ensemble typically relies on a complicated method that the whole QD ensemble are subdivided into N groups according to their characteristic interband transition energy; QDs belonging to the same group are supposed to be identical as shown in Fig. 1.4 and the probability of a QD belongs to a certain group follows a

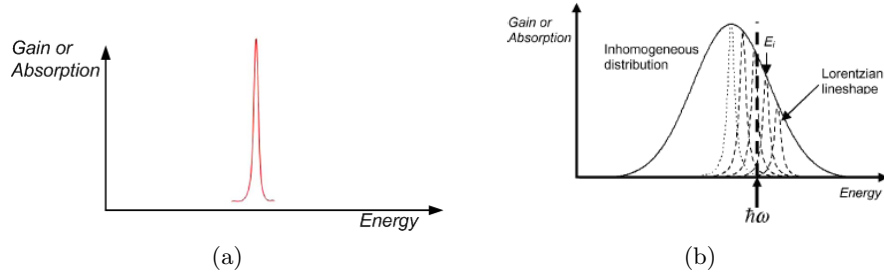


Figure 1.4: Schematics of the spectral gain profile for (a) single quantum dot and (b) an ensemble of self-assembled QDs grown by SK process.

Gaussian distribution. This is the multi-population method. Although this method could provide a complete description of the statistical distribution of the QD ensemble and the related spectral-domain properties, the computational cost of it is huge therefore limiting its efficiency in comprehensive analysis of QD-based devices. In order to reduce the computation demand to a reasonable value, in this thesis, the single-population approximation is utilized; we assume all the dots are identical in size, shape and consequently the gain spectrum profile, but the gain spectrum linewidth is as wide as the typical FWHM of an inhomogeneous broadened QD ensemble and the gain value at the characteristic lasing wavelength is also the same.

Successful generation of the QD layer is just the first step in the fabrication of a QD-based device. To form a feasible QD-based device where effective photon-carrier interaction happens, the self-assembled QD layer should be embedded in an appropriately designed multi-layer heterostructure. In next section, the epitaxial structure of the QD-based semiconductor devices will be introduced as well as the lateral patterning of the active region.

1.3 QD edge emitting devices

Practical semiconductor devices come to two basic classes: those with in-plane cavities and those with vertical cavities. In this thesis, only the first in-plane (or edge-emitting) type is considered. Figure 1.5 illustrates device of this type.

To fabricate a QD laser is much more than just simply substituting a QD active layer for the conventional QW layer. As suggested by Fig. 1.5, practical lasers must emit light in a narrow beam, which implies that the current, the carrier and the emitted photon have to be confined all in the same limited active region to maximize the interaction between the optical field and the active gain medium and increase the laser's efficiency. This condition has been achieved by several attempts in both the transversal y and the lateral x directions (see Fig. 1.5 for the definition of x and y

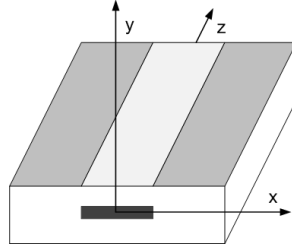


Figure 1.5: Simple schematic of edge-emitting lasers and the selected coordinate system of this thesis.

directions). The longitudinal optical propagation direction is designated as the z axis. This Cartesian coordinate system runs throughout this thesis.

To achieve larger gain and efficient carrier/photon collections in the transversal direction, following mechanism are commonly employed.

- Since the overall gain volume of a single QD layer is obvious significantly smaller than that of a single QW, multiple layers of QDs are stacked together. However, the accumulated strain from multiple QD layers causes defects in the active region. To overcome this issue, strain compensation layer (or spacer layer) with thickness of tens of nanometres (> 30 nm) is introduced between two adjacent QD layers.
- To effectively capture the electrons in the relatively small and spatially separated QDs, the so-called dots-in-a-well (DWELL) structure shows its advantage. As suggested by this structure, the dots are inserted in a quantum well so that the QW captures a high density of carriers and keeps them localized around the dots. Then, within the spontaneous emission lifetime of the captured carriers, they will relax into the confined states in QDs.
- Above mentioned thin QW carrier-confining active layer is surrounded by the *separate confinement* region with higher bandgap energy and smaller refractive index to confine the photons. This structure has been called as the separate confinement heterostructure (SCH).

As a distinct property of QD medium, its ground state (GS) emission wavelength can be easily controlled. By considering different III-V materials, the energy gap discontinuity between the QDs and the host material is engineered, tuning the 3D electronic potential well and consequently the GS emission wavelength in a certain range. For example, using InAs/In_xGa_{1-x}As QD heterostructure, GS emission from 1.1 to 1.3 μm can be achieved [22, 23].

In this thesis, we consider the devices grown on GaAs substrate and emitting around 1.3 μm . Consistently with above efficiency enhancement considerations, Fig. 1.6a shows schematically the epitaxial structure of a

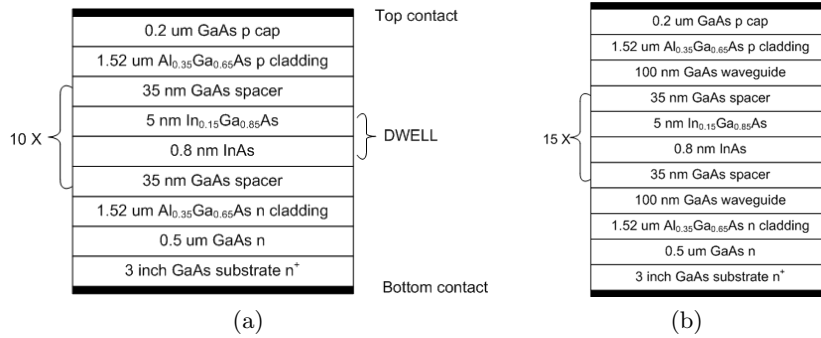


Figure 1.6: Schematics diagram of the epitaxial structure for InAs/InGaAs QD-based device with active region consisting of 10 stacks (a) and 15 stacks (b) of QD layers respectively.

typical InAs/InGaAs QD waveguide with 10 QD layers (QDLs). The active region consists of 10 stacks of self-assembled InAs QDs embedded in 5 nm of In_{0.15}Ga_{0.85}As quantum well layer and individual DWELL layers are separated by the 35-nm-thick GaAs spacer (or barrier) layers. The p and n cladding layers are constructed from 1520-nm-thick Al_{0.35}Ga_{0.65}As layers, forming the above mentioned SCH structure. Finally, as in conventional double heterostructure waveguides, a n-doped 500-nm-thick GaAs buffer layer on the bottom and a p-doped 200-nm-thick GaAs cap layer on the top of the heterostructure are considered, forming the p-type-intrinsic-n-type (p-i-n) junction for carrier injection. Above described heterostructure is grown on a 3-inch-thick GaAs substrate for mechanical reason.

The epitaxial structure for lasers with 15 QDLs is slightly different with that for lasers with 10 QDLs. As shown in Fig. 1.6b, the entire active region in 15 QDLs is sandwiched between two additional 100-nm-thick GaAs waveguides which then are followed by the cladding layers. Device with 5 QDLs are also studied in this thesis, which has similar epitaxial structure as that in the 15 QDLs case.

Figures 1.7a and 1.7b give a sketch of the energy gap and the refractive index variations along the growing direction (y) for the 10 QDLs case. The thin slab of undoped active region is sandwiched between p- and n-type cladding layers which have higher conduction-valence band energy gap. As illustrated in Fig. 1.7a, this simply p-i-n junction ensures that all the injected carriers recombine in the i-region (active region). Within the active region, thanks to the DWELL structure, a even lower transverse potential well is formed for electrons and holes injected under forward bias, and they are captured and confined together in a relatively small space to increase the probability of recombining with each other. The active region also has a higher refractive index than the cladding, as outlined in Fig. 1.7b, so that a transverse optical waveguide is formed, confining appropriately the optical

and interband transition energies in self-assembled QDs. These fundamental parameters of a QD device can be obtained through numerical calculation approaches, such as the software NextNano3D [25]. As an example, scheme of the energy band structure in above described InAs/In_{0.15}Ga_{0.85}As DWELL layers is shown in Fig. 1.8, and this energy level diagram is consistent with those reported in [26, 27, 28, 29]. We can see from Fig. 1.8b that three different confined QD states, the ground state (GS), the first excited state (ES) and the second excited state (ES_2) can be found in the conduction and the valence bands. Due to the spin degeneracy, these confined states are assumed to be two-fold ($D_{GS}=2$), four-fold ($D_{ES}=4$) and six-fold ($D_{ES_2}=6$) degenerate respectively. For energy higher than ES_2 , due to the finite confinement potential for real QDs, the energy levels tend to become closely spaced and highly degenerated and ultimately a transition to a continuum of delocalized states belonging to the WL or QW occurs. At even higher energies, a further transition towards 3D bulk states belonging to the barrier or SCH is achieved [25] (see Fig. 1.8a). In addition, if compare the energy band structure in the valence band with that in the conduction band, we can find that, in the valence band, the spacing between the confined states as well as the spacing between the confined states and the WL states are much smaller. These results can be attributed to the weakly confined hole wave functions and the larger heavy hole (HH) effective mass.

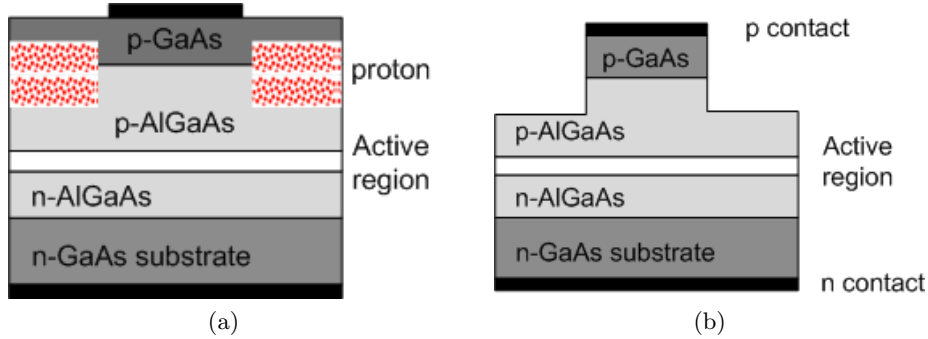


Figure 1.9: Cross-section view of the lateral confinement structures: (a) the proton-implant waveguide; (b) the ridge waveguide.

Up to now, we briefly described the transversal epitaxial structure and the associated energy band for QD-based devices. However, the lateral patterning of the active region is also necessary to increase device efficiency and reduce the threshold current. For the lateral direction confinement, two simple mechanisms are usually employed, the proton-bombarded waveguide (Fig. 1.9a) and the ridge waveguide (Fig. 1.9b). The former one offers some current confinements by implanting protons outside the waveguide region and thus creating damage and trapping out the mobile charges. This structure has been described as the *gain-guided* (GG) waveguide, and the optical

field guiding mechanisms in it will be studied in Chapter 4. The latter one, which has homogeneous core but complicated cross-section waveguide geometry, combines current confinement with a weak photon confinement by etching the outside region down to just above the active region. The etching depth can be adjusted to provide sufficient lateral refractive index change to form a single lateral mode optical waveguide. Therefore, this is the so-called *index-guided* (IG) waveguide and is used in the device discussed in Chapter 3. In both cases, carriers injected into the active region can diffuse laterally, decreasing partially the laser's efficiency.

1.4 Thesis outline

In this chapter, the basic properties of the considered QD-based edge-emitting device are described. To numerically simulate this kind of devices, the underlying physical mechanism of these properties should be described properly in the numerical models.

The thesis is organized as follows: in Chapter 2, the travelling wave equation which describes the field propagation in a optical waveguide, the rate equation system which describes the carrier dynamics in the QD active medium and the susceptibility equation which models the interaction between the electromagnetic field and the QD medium are introduced. They represent a complete description for a QD laser. Then two different numerical models are reported, allowing to solve above mathematical problems in different numerical approaches. In both models, we consider also the group velocity differences between the optical pulses from the GS and the ES transitions. Therefore, with respect to models available in the literature, these two models are capable to simulate special mode-locking lasers where GS and ES are lasing simultaneously.

In Chapter 3, the main results obtained in the simulation and analysis of the passively mode-locked QD lasers emitting around $1.3 \mu\text{m}$ are presented. After studying the general principles and analytical theories of passive mode-locking in semiconductor QD lasers, the above mentioned numerical models are extensively applied to analyze the mode-locked lasers and various useful design guidances of such devices are extracted. Particularly, simultaneous lasing from the fundamental GS transitions and the ES transitions in the QDs are investigated systematically.

In Chapter 4, the main works achieved in the modeling, simulation and design of QD semiconductor optical amplifiers are presented. The implemented numerical model based on the beam propagation method is introduced. This model is developed to model the static 2D variation of the electromagnetic field in the axially varying waveguide. By combining it with the results reported in Chapter 2, tapered optical amplifiers working at high power regime where nonlinear gain and refractive index variations are se-

vere can be simulated. Then different design methods have been exploited to obtain an optical amplifier which could supply high optical power amplification and good beam quality simultaneously. Furthermore, we show also other usages of this beam propagation method-based model in this chapter.

Finally, some conclusions are drawn and future plans are reported.

Chapter 2

QD-based edge-emitting dual-state laser modeling: basic principles and numerical models

In this thesis, various kinds of edge-emitting QD devices are considered. The schematic of a typical edge-emitting device and the corresponding general description have been depicted in previous Section 1.3. To correctly simulate such devices, reliable model that could transform the main underlying physical mechanisms within the devices to numerically solvable mathematical description is therefore needed.

In this chapter, two numerical models will be presented, both consist of a set of equations to be solved for the dynamic simulation of quantum dot based dual-state lasers. This equation set can be divided to three groups: in Section 2.1, the so-called travelling wave equation governing the spatio-temporal dynamics of the electromagnetic field propagating in the device is introduced, where terms representing the influence of the QD active medium on the electromagnetic field is appropriately included; then in Section 2.2, the carrier dynamics in the active medium is described via the rate equation system; in the subsequent Section 2.3, the coupling relationships between the electromagnetic field and the carriers, i.e., the optical field-induced polarisation and the spontaneous emission noise terms are explained. To numerically solve above equation set, in Section 2.4, a Finite Difference Travelling Wave (FDTW) model based on the finite difference scheme is depicted. This rigorous model supplies a complete description of the optoelectronic dynamics in the edge-emitting lasers and is also the most typically used method for simulations of such devices. However, the computational cost of this model is usually very high. In order to overcome this problem, a more efficient delayed differential equation (DDE) model is introduced in Section 2.5. These

two models are mainly applied to investigate the mode locking (ML) dynamics in the QD-based passively ML lasers studied in Chapter 3. Finally, a conclusion is drawn in Section 2.6.

2.1 Electromagnetic field dynamics

In this section, the main equations describing the amplitude evolution of an electromagnetic field propagating in the longitudinal direction of a optical ridge waveguide are presented. Since the derivation of such equations has already been shown in detail in many literatures, only the key results which are essential for understanding of the numerical models in this thesis are recalled. Readers who are interested to the clear explanation of the theoretical derivation can refer to the references listed along this review.

Without any doubt, the whole story starts from the Maxwell's equations for the electric field \vec{E} and magnetic field \vec{H} , which has the form as follows in frequency domain (ω)¹:

$$\nabla \times \vec{E} = -j\omega\mu\vec{H} \quad (2.1a)$$

$$\nabla \times \vec{H} = j\omega\epsilon\vec{E} \quad (2.1b)$$

where ϵ and μ denote the permittivity and permeability of the host medium. Taking into account the fact that we treat dielectric optical waveguide, we set the permeability as $\mu = \mu_0$. ϵ is related to its value in vacuum ϵ_0 by $\epsilon = \epsilon_0\epsilon_r(\omega, \vec{r}) = \epsilon_0n(\omega, \vec{r})^2$, where $\epsilon_r(\omega, \vec{r})$ is the spatial- and frequency-dependent relative dielectric constant of the background medium and $n(\omega, \vec{r})$ is the corresponding refractive index.

Equation (2.1) is considered in a lossless dielectric medium, for the active optical medium however, two additional terms governing the optical response of the medium should be included, and Maxwell's equations change to:

$$\nabla \times \vec{E} = -j\omega\mu_0\vec{H} \quad (2.2a)$$

$$\nabla \times \vec{H} = j\omega\epsilon_0\epsilon_r(\omega, \vec{r})\vec{E} + j\omega\vec{P}(\omega, \vec{r}) + \vec{J}(\omega, \vec{r}) \quad (2.2b)$$

where \vec{P} is the additional polarization induced by the semiconductor active medium including the changes in the gain and the refractive index of this medium and \vec{J} stands for a stochastic current density modeling the spontaneous emission noise from the active medium.

In order to solve Eq. (2.2), some approximations and assumptions are exploited to simplify it:

- For the particular case of a planar waveguide, two different sets of orthogonal modes which are usually referred as the transverse electric (TE) and the transverse magnetic (TM) modes satisfy Eq. (2.2)

¹A time propagation term $\exp(j\omega t)$ is exploited

[30, 31]; while for the ridge waveguide, although TE and TM modes cannot be strictly defined, one can find that the quasi-TE and quasi-TM modes are still supported by Eq. (2.2), which have small z -direction magnetic or electronic components respectively [32].

- Both the analytic derivation and the experiment findings [33, 34] show that quantum dots mainly interact with the TE-polarised field only and the quasi-TE emission is predominant in the QD edge-emitting devices. Therefore, only quasi-TE modes are considered in the following description.
- Most of the optical devices are designed to support only the fundamental guided mode at the operating frequency and cut off all the higher-order modes in both the transversal and the lateral direction, i.e., the so-called single mode waveguide design. Thus, in the following, we will focus on the dynamics of the fundamental quasi-TE mode. The propagation constant of that mode along the longitudinal direction z is expressed by $\beta(\omega) = \frac{\omega}{c}\eta(\omega)$, where c is the light velocity in a vacuum and $\eta(\omega)$ is the effective refractive index.

Considering the above aspects, one can finally obtain a second order differential equation for the z -dependent amplitude of the fundamental quasi-TE mode $E(z, \omega)$, where we ignore the details of the transverse field patterns:

$$\frac{\partial^2 E}{\partial z^2}(z, \omega) = -\frac{\omega^2}{c^2}\eta^2 E(z, \omega) - \omega^2 \mu_0 P(z, \omega) + j\omega \mu_0 J(z, \omega) \quad (2.3)$$

This equation is just a simple transmission line equation with additional terms for the optical response of the QDs and the spontaneous emission noise sources. If we assume a linear response of the semiconductor medium, the polarisation P can be computed through the electronic susceptibility $\chi(z, \omega)$:

$$P(z, \omega) = \epsilon_0 \Gamma_{xy} \chi(z, \omega) E(z, \omega) \quad (2.4)$$

where the field confinement factor Γ_{xy} is a parameter used to take into account the fact that the active region of the waveguide is only partially overlapped with the optical mode profile in both transversal and lateral direction; Γ_{xy} is defined as the ratio between the integration of the field overlapped with the active medium and the integration of the total field in the transversal plane. Additionally, the susceptibility χ is assumed to be constant within the active QD layers and depends on the z -direction position only.

Up to now, the variation of the mode amplitude in an optical semiconductor waveguide has been appropriately described. However, the typical

emitted light has the wavelength around 1 μm , and the corresponding frequency is about hundreds of THz. To numerically solve the temporal dynamics of such rapid system, huge computational cost is expected. Therefore, the slowly varying envelope approximation is commonly imposed. Since the mode amplitude $E(z, \omega)$ is usually characterized by a finite bandwidth centred at optical operating frequency ω_0 , so in the time domain, if we consider a device with Fabry-Perot cavity, the field amplitude $E(z, t)$ can be represented by the forward and backward propagating slowly varying components $E^+(z, t)$ and $E^-(z, t)$ according to:

$$E(z, t) = \sqrt{2\frac{\omega_0\mu_0}{\beta_0}} \left\{ E^+(z, t)e^{-j\beta_0 z} + E^-(z, t)e^{-j\beta_0 z} \right\} e^{j\omega_0 t} \quad (2.5)$$

where ω_0 is the optical carrier frequency of the electric field (usually referred to as the reference frequency) and β_0 is the corresponding propagation constant $\beta_0 = \frac{\omega_0}{c}\eta_0$ with $\eta_0 = \eta(\omega_0)$. In frequency domain Eq. (2.5) becomes to:

$$E(z, \omega_0 + \Omega) = \sqrt{2\frac{\omega_0\mu_0}{\beta_0}} \left\{ E^+(z, \Omega)e^{-j\beta_0 z} + E^-(z, \Omega)e^{-j\beta_0 z} \right\} \quad (2.6)$$

where Ω is defined as $\Omega = \omega - \omega_0$. Use this approximation the rapidly varying term $E(z, \omega)$ is replaced by the term $E(z, \Omega)$ with a much smaller variation rate and can be numerically solved more easily.

Similarly we define the slowly varying forward and backward travelling terms of the polarisation $P^\pm(z, t)$ and the spontaneous emission noise sources $J^\pm(z, t)$ respectively as:

$$P^\pm(z, t) = \epsilon_0 \bar{\chi}(t, z) \otimes E^\pm(t, z) = \epsilon_0 \int_{-\infty}^t \bar{\chi}(t - \tau, z) E^\pm(z, \tau) d\tau \quad (2.7a)$$

$$\bar{\chi}(t, z) = \frac{1}{2\pi} \int_{-\infty}^{+\infty} \chi(\omega_0 + \Omega, z) e^{j\Omega t} d\Omega = \chi(t, z) e^{-j\omega_0 t} \quad (2.7b)$$

where symbol \otimes represents a convolution product.

$$\begin{aligned} J^\pm(z, t) &= \frac{1}{2} \sqrt{\frac{\mu_0\omega_0}{2\beta_0}} \frac{1}{2\pi} \int_{-\infty}^{+\infty} J(\omega_0 + \Omega, z) e^{j\Omega t} d\Omega \\ &= \frac{1}{2} \sqrt{\frac{\mu_0\omega_0}{2\beta_0}} J(t, z) e^{-j\omega_0 t} \end{aligned} \quad (2.8)$$

Using Eqs. (2.5), (2.7) and (2.8) and doing the reverse Fourier transform of Eq. (2.3), one can finally obtain two independent first order differential equations for the forward and backward propagating field envelopes in time domain:

$$\pm \frac{\partial E^\pm}{\partial z} + \frac{1}{v_{g0}} \frac{\partial E^\pm}{\partial t} = -\frac{\alpha_i}{2} E^\pm - j \frac{\omega_0}{2c\eta_0\epsilon_0} \Gamma_{xy} P^\pm(z, t) + J^\pm(z, t) \quad (2.9)$$

where the group velocity is defined as:

$$\frac{1}{v_{g0}} = \frac{\eta_0}{c} \left(1 + \frac{\omega_0}{\eta_0} \frac{\partial \eta}{\partial \omega} \Big|_{\omega_0} \right) \quad (2.10)$$

In Eq. (2.9), we introduced an additional term accounting for the intrinsic waveguided losses α_i , which is induced by the doped atoms, contacts or defects in the waveguide. Equation (2.9) is the so-called travelling wave equation which is commonly used as a starting point to form the analytic or numerical model of the edge-emitting devices. For the Fabry-Perot cavity, the travelling field is reflected at the front and back facets of the cavity, Eq. (2.9) therefore should be combined with the boundary conditions at the facets, which show the coupling relationship between the forward and backward travelling fields. Such boundary conditions have simple forms as:

$$\begin{aligned} E^+(0, t) &= \sqrt{R_0} E^-(0, t) \\ E^-(L, t) &= \sqrt{R_L} E^+(L, t) \end{aligned} \quad (2.11)$$

where L is the total cavity length, R_0 and R_L are the power reflectivities at the device back and front facets respectively.

We want to stress here that $E^\pm(z, t)$ are properly normalized such that $|E^+(z, t)|^2$ and $|E^-(z, t)|^2$ simply give the total power flowing in the forward ($+z$) and backward ($-z$) directions in a certain longitudinal section of the device cavity.

In this section, fundamental equations determining the field propagation in a Fabry-Perot cavity waveguide are outlined. The travelling wave equation Eq. (2.9) and the coupled boundary conditions Eq. (2.11) should be solved to simulate the dynamics of the temporal-spatio dependent field envelope $E^\pm(z, t)$. To do so, the polarisation and the spontaneous emission noise induced by the active medium should be explicitly described; these terms tightly relate with the carrier distributions in the corresponding QD states in the active medium, and these carrier distributions are also temporal-spatio dependent due to their interaction with the electric fields. Thus, in next section, the so-called rate-equation system describing the carrier occupation probabilities in the QD confined states, the WL and the SCH is introduced.

2.2 Carrier dynamics in the active medium

In this section, carrier generation, recombination and moving mechanisms in the QD active medium will be described numerically in a rigorous way and summarized in the so-called rate-equation system, which governing the temporal dynamics of the carrier distributions in different energy levels of the self-assembled QDs.

In Fig. 2.1, we show schematically the simplified band structure of a typical InAs/InGaAs QD semiconductor material. Consistently with the

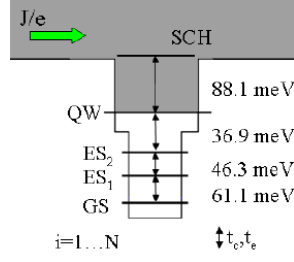


Figure 2.1: Schematic of the cascade transitions of electrons between different states in the conduction band of the QD material. Arrows indicate the capture/relaxation and escape processes of electrons.

description in Section 1.3, 3 discrete energy levels within the QD are considered (GS , ES , ES_2).

As always, following assumptions and approximations are exploited to limit the computational cost of this model reasonably low.

- We assume the charge neutrality condition in each QD confined state, in the QW and also in the SCH, which means the electron number in these states in the conduction band equals exactly to the hole number in the corresponding states in the valence band. Using this approximation, the model actually treats with the dynamics of the correlated electron-hole pairs in the different states, and therefore is usually referred to as the excitonic model. Thus, in the following, only the electron dynamics in the conduction band are computed. This approach is also commonly encountered in literatures [35, 36, 37, 38].
- As pointed out in Section 1.3, the three confined QD energy levels have degeneracy of 2, 4 and 6 respectively. In our model, we assume that the degenerate states in each energy level have identical population dynamics and interact in the same way with the electromagnetic field.
- As shown in Section 1.2, due to the inherent property of the self-assembled QD medium, the QDs are not identical but have a distribution in terms of the size, the shape and the composition. All these aspects lead to a dispersion in the optical interband transition energies of the QDs and therefore the QD ensembles show a significant inhomogeneous broadened gain spectrum. A full description of such complex system needs to divide the whole QD ensembles to several subgroups assuming the QDs are identical in each subgroup. Then, 3 rate equations related the confined QD states should be considered for each subgroup. However, in this thesis, above approach is significantly simplified via the single-population approximation. In detail, we assume that only one group of QDs exist, which means the whole QD

ensembles are identical and the characteristic FWHM of the homogeneous broadened gain profile of this single QD group is as large as the original highly broadened gain entire spectrum (about 34 meV). Thus only 3 rate equations are used to represent the carrier dynamics in the *GS*, the *ES* and the *ES₂*.

- In many papers [36, 37, 39, 27], carrier capture and relaxation from the higher energy level towards the lower energy level are assumed to exist only between adjacent states and there is no scattering from SCH directly to the QD confined states. We follow also this approach so that carriers are captured and relaxed from the 3D SCH to the QD GS as a cascade process, as shown in Fig. 2.1.
- There is a huge set of delocalized states existing in the 2D QW and 3D barrier (SCH), and one equation for modeling the population dynamics of one such state should be considered [40, 41]. In the following, we assume that the carriers belonging to the QW states are always under a quasi-equilibrium condition, which is equivalent to say that the electrons in the QW conduction band states satisfy a Fermi distribution defined by the electron quasi-Fermi level; the same condition also happens for the electrons in the SCH states. This approximation is possible because the scattering processes driving such two systems towards Fermi distribution occur usually in a very short time scale (30 - 50 fs) [40], which is much shorter than the optical dynamics we concerned. Therefore, carrier dynamics in the QW and SCH states are described only by two coupled rate equations for the total electron densities there. We have to stress that the quasi-equilibrium distribution is assumed only in the WL and the barrier, while in the QD confined states the carrier populations are far from the equilibrium condition.

2.2.1 Rate equation system for the current injection section

Follow these approximations, the whole set of rate equations modeling the carrier dynamics in the entire QD system in forward bias condition (pumping current injection) can be written as:

$$\begin{aligned} \frac{\partial n_{SCH}}{\partial t} = & \eta_i \frac{J}{e} W - \frac{n_{SCH}}{\tau_{SCH \rightarrow QW}} + \frac{n_{QW}}{\tau_{QW \rightarrow SCH}} \\ & - \frac{n_{SCH}}{\tau_{nr, SCH}} \end{aligned} \quad (2.12)$$

$$\begin{aligned} \frac{\partial n_{QW}}{\partial t} = & \frac{n_{SCH}}{\tau_{SCH \rightarrow QW}} - \frac{n_{QW}}{\tau_{QW \rightarrow SCH}} - \frac{n_{QW}}{\tau_{nr, QW}} \\ & + \frac{n_{QW} (1 - \tilde{f}_{ES_2})}{\tau_{QW \rightarrow ES_2}} + \frac{n_{ES_2}}{\tau_{ES_2 \rightarrow QW}} \end{aligned} \quad (2.13)$$

$$\begin{aligned} \frac{\partial n_{ES_2}}{\partial t} = & \frac{n_{QW} (1 - \tilde{f}_{ES_2})}{\tau_{QW \rightarrow ES_2}} - \frac{n_{ES_2}}{\tau_{ES_2 \rightarrow QW}} \\ & - \frac{n_{ES_2}}{\tau_{ES_2 \rightarrow ES}} (1 - \tilde{f}_{ES}) + \frac{n_{ES}}{\tau_{ES \rightarrow ES_2}} (1 - \tilde{f}_{ES_2}) \\ & - \frac{n_{ES_2}}{\tau_{sp, ES_2}} - \frac{n_{ES_2} \tilde{f}_{ES_2}}{\tau_{Aug, ES_2}} - \frac{n_{ES_2}}{\tau_{nr, ES_2}} - R_{st, ES_2} \end{aligned} \quad (2.14)$$

$$\begin{aligned} \frac{\partial n_{ES}}{\partial t} = & \frac{n_{ES_2}}{\tau_{ES_2 \rightarrow ES}} (1 - \tilde{f}_{ES}) - \frac{n_{ES}}{\tau_{ES \rightarrow ES_2}} (1 - \tilde{f}_{ES_2}) \\ & - \frac{n_{ES}}{\tau_{ES \rightarrow GS}} (1 - \tilde{f}_{GS}) + \frac{n_{GS}}{\tau_{GS \rightarrow ES}} (1 - \tilde{f}_{ES}) \\ & - \frac{n_{ES}}{\tau_{sp, ES}} - \frac{n_{ES} \tilde{f}_{ES}}{\tau_{Aug, ES}} - \frac{n_{ES}}{\tau_{nr, ES}} - R_{st, ES} \end{aligned} \quad (2.15)$$

$$\begin{aligned} \frac{\partial n_{GS}}{\partial t} = & \frac{n_{ES}}{\tau_{ES \rightarrow GS}} (1 - \tilde{f}_{GS}) - \frac{n_{GS}}{\tau_{GS \rightarrow ES}} (1 - \tilde{f}_{ES}) \\ & - \frac{n_{GS}}{\tau_{sp, GS}} - \frac{n_{GS} \tilde{f}_{GS}}{\tau_{Aug, GS}} - \frac{n_{GS}}{\tau_{nr, GS}} - R_{st, GS} \end{aligned} \quad (2.16)$$

where $R_{st,k}$ ($k = GS, ES, ES_2$) in Eqs. (2.14), (2.15) and (2.16) represent the stimulated emission/absorption rates from each QD state, J in 2.12 is the applied current density and η_i is the internal quantum efficiency.

In above rate equations, $n_{SCH}(z, t)$, $n_{QW}(z, t)$ and $n_k(z, t)$ ($k = GS, ES, ES_2$) are the total number of electron per unit length in the barrier (SCH), QW and the confined QD states respectively. Among them, the $n_k(z, t)$ can be simply related to the corresponding occupation probabilities (averaged over the transversal direction) $\tilde{f}_k(z, t)$ via the following expression:

$$n_k(z, t) = \tilde{f}_k(z, t) W N_{lay} N_d D_k \quad (2.17)$$

where N_{lay} is the number of stacked QD DWELL layers, N_d is the QD surface density, W is the ridge width and D_k is the degeneracy of the k^{th} state.

$R_{st,k}$ can be calculated as follows:

$$R_{st,k} = -\frac{j}{\hbar} \frac{N_d}{H_w} \frac{D_k}{\epsilon_0 c \eta_0} \text{Im} \left\{ d_{x,k} E^+ p_k^{+,*} + d_{x,k} E^- p_k^{-,*} \right\} \quad (2.18)$$

where H_w is the width of the QW layer, p_k^\pm is the slowly varying microscopic interband polarisation and $d_{x,k}$ is the x-component of the dipole matrix element. The latter two terms will be explained later in Section 2.3.

The time constant $\tau_{SCH \rightarrow QW}$ represents the characteristic capture time from the barrier states into the QW states. This quantity actually is the sum of the characteristic time for carrier diffusion across the SCH region and the capture in the QW states i.e. $\tau_{SCH \rightarrow QW} = \tau_{diff} + \tau_{cap}$. The diffusion time τ_{diff} , which relates directly to the width of SCH (H_{SCH}), can be calculated from the electron mobility in the conduction band as reported in [27].

QD relaxation times $\tau_{QW \rightarrow ES_2}$, $\tau_{ES_2 \rightarrow ES}$ and $\tau_{ES \rightarrow GS}$ governing the intraband dynamics of electrons are usually in the range of few picoseconds. Unlike the sophisticated approaches used in [42], in this work, these characteristic times are assumed to be a constant and independent on the QW carrier densities, allowing therefore to significantly reduce the complexity of the rate equation system. In addition, due to the highly reduced density of states, we take into account the Pauli exclusion principle in the expression for the electron relaxation rate $R_{k \rightarrow k'}(\tilde{f}_k, \tilde{f}_{k'})$ (k and k' represent the initial and the final states respectively) in the QD states as:

$$R_{k \rightarrow k'}(\tilde{f}_k, \tilde{f}_{k'}) = \frac{\tilde{f}_k(z, t) (1 - \tilde{f}_{k'}(z, t))}{\tau_{k \rightarrow k'}} \quad (2.19)$$

whereas this Pauli exclusion principle do not need to be considered if the final state k' is within the WL or the SCH.

Furthermore a relation between the out scattering rate $R_{k \rightarrow k'}(\tilde{f}_k, \tilde{f}_{k'})$ and the opposite in scattering rate $R_{k' \rightarrow k}(\tilde{f}_{k'}, \tilde{f}_k)$ should also be considered. In the condition that no external perturbations exist, electrons population would tend to be a quasi-equilibrium distribution within the conduction band states, i.e., a Fermi distribution with a given quasi-Fermi level. To ensure this kind of quasi-equilibrium distribution, the detailed balance condition between carrier relaxation and excitation processes involving the same pair of initial and final states must be imposed:

$$\frac{\tau_{k \rightarrow k'}}{\tau_{k' \rightarrow k}} = \exp \left(\frac{\hbar \omega_{k'} - \hbar \omega_k}{k_B T} \right) \quad (2.20)$$

where $\hbar \omega_k$ is the interband transition energy of each state.

Equation (2.20) represents the detailed balance condition. Based on it, the electron escape characteristic time constants can be related with the

corresponding capture and relaxation times via the following expressions:

$$\frac{\tau_{QW \rightarrow SCH}}{\tau_{SCH \rightarrow QW}} = \frac{DOS_{QW} N_{lay}}{DOS_{SCH} H_{SCH}} \exp\left(\frac{\hbar\omega_{SCH} - \hbar\omega_{QW}}{k_B T}\right) \quad (2.21a)$$

$$\frac{\tau_{ES_2 \rightarrow QW}}{\tau_{QW \rightarrow ES_2}} = \frac{D_{ES_2} N_d}{DOS_{QW}} \exp\left(\frac{\hbar\omega_{QW} - \hbar\omega_{ES_2}}{k_B T}\right) \quad (2.21b)$$

$$\frac{\tau_{ES \rightarrow ES_2}}{\tau_{ES_2 \rightarrow ES}} = \frac{D_{ES}}{D_{ES_2}} \exp\left(\frac{\hbar\omega_{ES_2} - \hbar\omega_{ES}}{k_B T}\right) \quad (2.21c)$$

$$\frac{\tau_{GS \rightarrow ES}}{\tau_{ES \rightarrow GS}} = \frac{D_{GS}}{D_{ES}} \exp\left(\frac{\hbar\omega_{ES} - \hbar\omega_{GS}}{k_B T}\right) \quad (2.21d)$$

where DOS_{SCH} and DOS_{QW} are the effective density of states in the QW and SCH that can be calculated as:

$$DOS_{SCH} = 2 \left(\frac{2\pi m_{SCH}^* k_B T}{\hbar^2} \right) \quad (2.22a)$$

$$DOS_{QW} = \frac{m_{QW}^* k_B T}{\pi \hbar^2} \quad (2.22b)$$

being m_{QW}^* and m_{SCH}^* the electron effective masses in the InGaAs QW and the GaAs barrier. The effective density of states DOS_k ($k = SCH, QW$) and the QD state degeneracies D_k appear in Eq. 2.21 in order to properly account for the transitions between all the possible initial and final states of the system.

Up to now the intraband scattering processes for carriers in the QD system have been introduced, represented by the rate $R_{k \rightarrow k'}(\tilde{f}_{k'}, \tilde{f}_k)$ and the characteristic time $\tau_{k \rightarrow k'}$ of them. These processes guarantee the quasi-equilibrium electron distribution within the conduction band states represented by a separate quasi-Fermi level within the conduction band. Besides them, an additional rate $R^{rec}(\tilde{f}_k)$ has also been included to account for the interband recombination processes which ensure the thermodynamic equilibrium between the electrons and holes leading to a common Fermi-energy within the band gap when there is no any external excitations, such as the current or optical field pumping. The total interband recombination rate consists of the contributions from the spontaneous emission, the non-radiative recombination and the Auger recombination. That is:

$$R_k^{rec} = R_k^{sp} + R_k^{Au} + R_k^{nr} \quad (2.23)$$

The spontaneous emission involves the recombination of an electron-hole pair and give rise to the emission of a photon simultaneously. The spontaneous emission rate can be written as:

$$R_k^{sp}(\tilde{f}_k) = \frac{1}{\tau_{sp,k}} \tilde{f}_k \quad (2.24)$$

where $\tau_{sp,k}$ is the characteristic spontaneous emission time constant. This value can be related to the dipole matrix element of the considered interband transitions as will be described in Subsection 2.3.2.

The non-radiative recombination actually is a monomolecular recombination due to deep level traps located within the band gap of the semiconductor material and it can be modelled simply as:

$$R_k^{nr} = \frac{\tilde{f}_k}{\tau_{nr,k}} \quad (2.25)$$

where $\tau_{nr,k}$ is the characteristic time constant.

Finally, the Auger recombination involves the recombination of an electron-hole pair and the excitation of either an electron or a hole towards higher energy states (usually 2D quantum well states or barrier states). In this work, Auger recombination has been taken into account as:

$$R_k^{Aug} = \frac{1}{\tau_{Aug,k}} (\tilde{f}_k)^2 \quad (2.26)$$

where $\tau_{Aug,k}$ is the characteristic time constant.

For the QD confined states, non-radiative recombination and spontaneous emission recombination have characteristic rate which are usually much larger than that for Auger recombinations. Therefore, Auger recombination is usually the dominant interband recombination path [43],[44].

Equations (2.12)-(2.16) represent a complete system of equations describing the carrier dynamics within the QD system in each section of a waveguide under current injection. While, in many photonic devices, such as the passively mode-locked lasers and modulators, a section which is under reverse voltage bias is considered also. Therefore, in next subsection, we depict the modifications in the rate equation system in order to take into account the influence of the reverse bias voltage.

2.2.2 Rate equation system for the reverse biased section

In the reverse biased QD waveguide (the so-called saturable absorber, SA), a static electric field which is perpendicular to the QD layers (y direction) is applied to the p-i-n junction leading to significant changes in the optical properties of the QD material. The effect of an applied static field on the QD material is threefold:

- Leading to a lowering of the barrier height between the SCH and the QW states and between the QW and the ES_2 states. The carrier escape rates from the lower energy states to the higher energy states are enhanced.

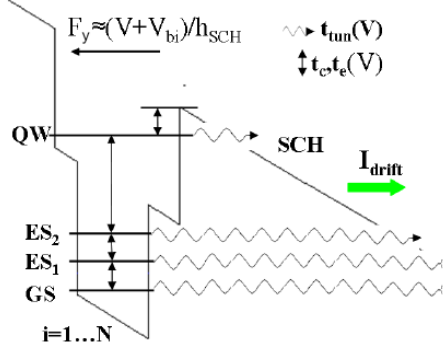


Figure 2.2: Schematic of the energy diagram in a reverse bias condition. Symbol \rightsquigarrow denotes tunneling processes. Double arrows \updownarrow indicate possible capture (relaxation) and escape processes.

- Leading to the formation of a triangular barrier, and the width of this triangle may be significantly decreased to allow carrier tunneling from the QW states and the confined QD states to the SCH states at high applied field. This represents an additional carrier sweep-out path.
- Leading to a small red-shift of the characteristic transition energies for carriers in the QD medium due to the weak Quantum Confinement Stark Effect (QCSE).

Therefore, it is essential to modify accordingly the rate equations in previous subsection (2.12-2.16) to properly describe the carrier dynamics in a reversely biased active region. A schematic of the possible modified intraband transitions is shown in Fig. 2.2.

The intraband carrier dynamics within the QD states are significantly influenced by static electric field. First, this reverse field results in a reduction in the original potential barrier, therefore, an enhanced thermionic escape from the QD states to the WL and SCH states occurs [45]. The electric field F_y can be simply related to the reverse voltage according to $F_y = \frac{V+V_{bi}}{H_{SCH}}$, where $V_{bi} > 0$ is the built-in potential of the junction, $V > 0$ is the applied voltage and H_{SCH} is the width of the separate confinement heterostructure. And the linear reduction in the confinement potential barrier can be estimated simply as $\frac{1}{2}F_y H_w$, where H_w is the width of the QW layers. Then the electric field dependent escape times can be simply modelled via following modified expressions for the original characteristic escape times ($\tau_{QW \rightarrow SCH}(0)$, $\tau_{ES_2 \rightarrow QW}(0)$ when $F_y = 0$):

$$\begin{aligned} \tau_{QW \rightarrow SCH}(F_y) &= \tau_{QW \rightarrow SCH}(0) \exp\left(-\frac{eF_y H_w}{k_B T}\right) \\ \tau_{ES_2 \rightarrow QW}(F_y) &= \tau_{ES_2 \rightarrow QW}(0) \exp\left(-\frac{eF_y H_w}{k_B T}\right) \end{aligned} \quad (2.27)$$

Furthermore, at sufficiently high reverse voltages, the induced slope in the band structure allows for efficient tunneling processes of electrons from the QD and QW states towards the bulk SCH states [46, 45]. These tunneling escape rates can be estimated using the Wentzel-Kramer-Brillouin approximation for a triangular well [45], [47]:

$$\begin{aligned} R_{tun,k}(z,t) &= f_{tun} \exp\left(-\frac{4}{3} \frac{\sqrt{2m_{SCH}^*}(\hbar\omega_{SCH} - \hbar\omega_k)^{\frac{3}{2}}}{e\hbar F_y}\right) n_k(z,t) \\ R_{tun,QW}(z,t) &= f_{tun} \exp\left(-\frac{4}{3} \frac{\sqrt{2m_{SCH}^*}(\hbar\omega_{SCH} - \hbar\omega_{QW})^{\frac{3}{2}}}{e\hbar F_y}\right) n_{QW}(z,t) \end{aligned} \quad (2.28)$$

where $f_{tun} = \frac{\hbar\pi}{2m^*H_w^2}$ is the characteristic barrier collision frequency for electrons and $k = GS, ES, ES_2$.

Above described enhanced thermionic escape rates and the additional tunneling processes were found to be the main influences in the intraband carrier dynamics induced by the an applied electric field. However, the interband carrier dynamics are also influenced by the reverse voltage. The QCSE which has been previously observed in QW devices has also been clearly observed in QD systems [46]. This effect leads to the modifications in the QD wave functions and therefore the shift in the characteristic interband transition energies from the QD states [46], [48]. However, the strength of this effect is significantly smaller than that in quantum wells. In our model, the QCSE in reverse biased saturable absorber based on QDs is neglected. To model carrier dynamics in the reversely biased junction we need therefore to introduce in the rate equation system Eqs. (2.12)-(2.16) the expressions for the electric field dependent characteristic escape times Eq. (2.27) and for tunneling rates Eq. (2.28).

Finally, due to the applied electric field, carriers in the intrinsic barrier region are quickly swept out from the active region. Such additional drift current should be introduced in the modified rate equation for carriers in the SCH:

$$\begin{aligned} \frac{\partial n_{SCH}}{\partial t} &= -\frac{\mu_d F_y n_{SCH}}{H_{SCH}} - \frac{n_{SCH}}{\tau_{SCH \rightarrow QW}} + \frac{n_{QW}}{\tau_{QW \rightarrow SCH}} \\ &- \frac{n_{SCH}}{\tau_{nr,SCH}} + \sum_k R_{tun,k} + R_{tun,QW} \end{aligned} \quad (2.29)$$

where μ_d represents the GaAs electron mobility and $k = GS, ES, ES_2$.

In this section, a complete rate equation system have been established for QD-based waveguide under current injection or reverse voltage bias. These equations link the carrier dynamics in the QD system with the microscopic

polarisations $p_k^\pm(z, t)$ through the stimulated emission terms (Eq. (2.18)). While in Section 2.1, the introduced travelling wave equation Eq. (2.9) supply a link between the electromagnetic field dynamics with the QD optical response through a macroscopic polarisation term. Therefore, what are still missing are the expressions for the micro/macro polarisation terms and the relation between them. Furthermore, the spontaneous emission noise which is another link path between the travelling wave equation (2.9) and the rate equation system (Eqs. (2.14) - (2.16)) should also be properly considered. In next section, these problems will be solved.

2.3 Interaction between the electromagnetic field and the active medium

In this section, we will introduce the quantum mechanical description of the optical properties of the semiconductor QDs.

2.3.1 Polarisation induced by an electromagnetic field

The optical response of each QD to an electromagnetic field can be solved from the density-matrix theory. Follows this approach the coherent and incoherent dynamics induced by the external optical field in microscopic interband polarisation can be described as [40], [35]:

$$\left(\frac{d}{dt} - j\omega_k + \Gamma \right) p_k(t) = +\frac{j}{\hbar} \vec{E} \cdot \vec{d}_k (2f_k(t) - 1) \quad (2.30)$$

In Eq. (2.30), we actually consider the microscopic interband polarisation as a dephasing process and $1/\Gamma$ is the characteristic dephasing time (also can be understood as the FWHM of the homogeneous broadened gain spectrum). It is clearly shown that the QD p_k depends on the local electric field \vec{E} . Therefore, consistently with what we already did for the \vec{E} in Section 2.1, the elimination of the transverse coordinates (x, y) dependence and the slowly varying approximation are also introduced to p_k and the slowly varying microscopic interband polarisations p_k^\pm are defined as:

$$\begin{aligned} & \sqrt{\frac{2\omega_0\mu_0}{\beta_0}} \left(p_k^+(z, t)e^{-j\beta_0 z} + p_k^-(z, t)e^{+j\beta_0 z} \right) e^{j\omega_0 t} = \\ & = \iint p_k(x, y, z, t) e_x'^*(x, y) dx dy \end{aligned} \quad (2.31)$$

And the corresponding slowly varying macroscopic polarisation $P^\pm(z, t)$ in Eq. (2.9) can then be written as:

$$\Gamma_{xy} P^\pm(z, t) = \frac{N_d}{h_w} \sum_{k=GS, ES, ES_2} 2d_{x,k}^* p_k^\pm(z, t) \quad (2.32)$$

Equation (2.7) allows to establish a connection between the classical theory of the electromagnetic wave propagation in a optical waveguide described in Section 2.1 and the optical properties of the QD ensembles.

Furthermore, the definition equation for the slowly varying polarisations p_k^\pm change to:

$$\begin{aligned} \frac{\partial p_k^\pm}{\partial t}(z, t) = & (j(\omega_k - \omega_0) - \Gamma) p_k^\pm(z, t) + \\ & + \frac{j}{\hbar} \Gamma_{xy} d_{x,k} \left(2\tilde{f}_k(z, t) - 1 \right) E^\pm(z, t) \end{aligned} \quad (2.33)$$

Comparing with respect to Eq. (2.30), we stress that in this equation ω_0 is the selected reference frequency and additionally the field confinement factor Γ_{xy} is introduced to describe the incomplete overlap between the transverse guided mode and the QD active layers.

By performing Fourier and inverse Fourier transforms of Eq. (2.33), exploiting the fact that polarisation dephasing time ($1/\Gamma \simeq 100$ fs) is much faster than the occupation probability dynamics in the QD states (the adiabatic approximation) and using Eq. (2.32), we can rewrite the expression for $P^\pm(z, t)$ as:

$$\begin{aligned} \Gamma_{xy} P^\pm(z, t) = & \Gamma_{xy} \sum_k \frac{D_k N_d j |d_{y,k}|^2}{H_w \hbar \Gamma} \\ & \left(2\tilde{f}_k(z, t) - 1 \right) [\mathcal{L}_k(t) \otimes E^\pm(z, t)] \end{aligned} \quad (2.34)$$

where \mathcal{L}_k is a complex Lorentzian function centred at frequency $\omega_k - \omega_0$, being ω_k the center interband transition frequency of state k . The frequency domain and time domain forms of this Lorentzian function are:

$$\mathcal{L}_k(\Omega) = \frac{1}{1 + j \frac{\Omega - \omega_k + \omega_0}{\Gamma}} \quad (2.35)$$

$$\mathcal{L}_k(t) = \Gamma \exp(j(\omega_k - \omega_0)t) \exp(-\Gamma t) \quad (2.36)$$

Comparing to previous definition of the susceptibility Eq. (2.7), we can therefore define the slowly varying QD susceptibility as:

$$\bar{\chi}(t, z) = \sum_k \frac{D_k N_d j |d_{x,k}|^2}{H_w \epsilon_0 \hbar \Gamma} \cdot \left(2\tilde{f}_k(z, t) - 1 \right) \mathcal{L}_k(t) \quad (2.37)$$

And the time varying QD gain and refractive index spectra which are tightly related to the imaginary and real parts of the susceptibility of the

QD system are defined as follows:

$$\begin{aligned} g(z, t, \Omega) &= \frac{\omega_0}{c\eta_0} \text{Im} \{ \bar{\chi}(z, t, \Omega) \} = \\ &= \sum_k g_{0,k} \cdot \left(2\tilde{f}_k(z, t) - 1 \right) \text{Re} \{ \mathcal{L}_k(\Omega) \} \end{aligned} \quad (2.38)$$

$$\begin{aligned} \Delta\eta(z, t, \Omega) &= \frac{1}{2\eta_0} \text{Re} \{ \bar{\chi}(z, t, \Omega) \} \\ &= - \sum_k \frac{c}{\omega_0} g_{0,k} \cdot \left(2\tilde{f}_k(z, t) - 1 \right) \text{Im} \{ \mathcal{L}_k(\Omega) \} \end{aligned} \quad (2.39)$$

where we defined:

$$g_{0,k} = \frac{\omega_0 D_k N_d |d_{x,k}|^2}{c\eta_0 H_w \epsilon_0 \hbar \Gamma} \quad (2.40)$$

$g_{0,k}$ is the gain coefficient in each QD state. It is one of the most important parameters in the simulation and is usually obtained by fitting the experimental measured gain or absorption spectrum.

Equations (2.37), (2.38) and (2.39) can be mathematically explained as that, the optical response of the QD active medium can be described by the filtering of the electromagnetic field via different Lorentzian filters associated to each interband transition from QDs. The FWHM of the Lorentzian function is given by 2Γ . Therefore, it is proportional to the dephasing rate for the microscopic interband polarisation. Usually, we call this broadening mechanism the homogeneous broadening. We emphasize again that the inhomogeneous broadening mechanism is neglected in the simple model (see Section 1.2).

Through above derivations, one can couple directly the travelling wave equation Eq. (2.9) with the rate equation system describing carrier dynamics in the QD layers (Eqs. (2.12)-(2.16)) through the QD susceptibility Eq. (2.37), therefore eliminating the equations for the microscopic polarisations. To this end, the stimulated emission/absorption rate appearing in the rate equation system can be written as follows:

$$\begin{aligned} R_{st,k} &= \frac{\Gamma_{xy}}{\hbar\omega_0} g_{0,k} \left(2\tilde{f}_k(z, t) - 1 \right) \cdot \\ &\quad \text{Re} \left\{ E^+(z, t) [\mathcal{L}_k(t) \otimes E^+(z, t)]^* + E^-(z, t) [\mathcal{L}_k(t) \otimes E^-(z, t)]^* \right\} \end{aligned} \quad (2.41)$$

Up to now, the first term (polarisation) in the travelling wave equation Eq. (2.9) has been successfully solved and coupled to the rate equation system. We will complete the whole model by introducing proper expression for the second term in Eq. (2.9) (the spontaneous emission noise source) in next subsection.

2.3.2 Spontaneous emission noise

Spontaneous emission is one of the major recombination processes of electrons and holes injected in the QD layers. We need a proper description of the spontaneous emission mechanism which links the phenomenological spontaneous emission rate Eq. (2.24) characterized by the recombination time $\tau_{sp,k}$ in the rate equation system and the effective current density $J^\pm(z, t)$ describing spontaneous emission noise in the travelling wave equation Eq. (2.9) must be considered.

Unlike the rigorous treatment of the spontaneous emission noise in semiconductors in [49] and [50], we obtain the expression for the power spectral density of the spontaneous emission from the expression of the QD gain spectrum Eq. (2.38), following the Einstein theory in Appendix 6 (pp. 459-472) of Coldren's book [51]. The spontaneously emitted power per unit length, per unit bandwidth, generated from the QD ensemble in one longitudinal section of the device, and coupled with the transverse guided mode can be written as:

$$\begin{aligned} |J^\pm(z, \Omega)|^2 &= \frac{\beta_{sp}}{2} N_d W N_{lay} \sum_k D_k \frac{\Gamma \hbar \omega_k}{\pi} R_{sp,k}(z, t) \text{Re} \{ \mathcal{L}_k(\Omega) \} \\ &= \frac{\beta_{sp}}{2} N_d W N_{lay} \sum_k D_k \frac{\Gamma}{\pi} \frac{\hbar \omega_k R_{sp,k}(z, t)}{1 + \left(\frac{\Omega - \omega_k + \omega_0}{\Gamma} \right)^2} \end{aligned} \quad (2.42)$$

where $R_{sp,k}$ is the spontaneous emission rate as in Eq. (2.24); β_{sp} is the spontaneous emission coupling factor which takes into account the fact that only a small fraction of the total spontaneously emitted radiation couples with the transverse mode of the optical waveguide (typical values for β_{sp} are around $10^{-3} - 10^{-4}$); the factor $\frac{1}{2}$ appearing in Eq. (2.42) is due to the assumption that half of the spontaneous emission couples with the guided mode propagating along the forward direction and half couples with that along the backward direction.

In this subsection, we have provided an expression for the power spectral density of the spontaneous emission noise source appearing in the travelling wave equations, and it has been coupled with the spontaneous emission rate term in the travelling wave equation. So far, complete description of the electromagnetic field dynamics and the carrier dynamics in a QD-based device have been presented. In next section, we introduce therefore how to solve this equation set numerically.

2.4 Single-population dual-state FDTW model

The finite difference travelling wave model actually represents a full description of the dynamics happening in the self-assembled QD-based lasers. This model bases on the direct solution of the travelling wave equation Eq.

(2.9) through the finite difference scheme where the polarisation and the spontaneous emission terms supply links between the intracavity circulating electromagnetic fields and the intracavity carriers. In the following, we consider a Fabry-Perot (FP) laser with the active region consisting of multiple InAs QD layers and emitting around $1.3 \mu m$ and use it as a example to describe the FDTW model.

In the FDTW model, we consider only the optical responses arising from the QD GS and ES, since we assume that the contributions from higher QD states are significantly detuned with respect to the main lasing frequencies and therefore can be neglected. Consequently the optical field E^\pm is split into two uncoupled parts E_k^\pm ($k = GS \text{ or } ES$), one for the GS and one for the ES, and each one propagates in the laser cavity with its own group velocity $V_{g,k}$. In order to correctly describe the dynamics of the optical fields generated from two states with distinct wavelengths, it is essential to include also the group velocity differences between these two fields in the numerical model. Therefore two travelling wave equations are solved at the GS and ES wavelengths respectively ($k = GS \text{ or } ES$):

$$\pm \frac{\partial E_k^\pm}{\partial z} + \frac{1}{v_{g0,k}} \frac{\partial E_k^\pm}{\partial t} = -\frac{\alpha_i}{2} E_k^\pm - j \frac{\omega_0}{2c\eta_0\epsilon_0} \Gamma_{xy} P_k^\pm(z, t) + J_k^\pm(z, t) \quad (2.43)$$

QD optical susceptibility

The field-induced polarisation actually indicates the variation in the optical field through the susceptibility. The real and imaginary parts of the optical susceptibility correspond to the refractive index changes and the gain respectively. The former parameter induces variation in the phase of the optical field, whereas the latter parameter induces variation in the amplitude of the optical field.

As pointed out just before, there are two separate optical fields, therefore the optical responses in terms of the gain and the refractive index changes should be considered also separately. So the total gain/refractive index spectrum consists of two distinct bands, as shown in Fig. 2.3. This approximation can significantly reduce the simulation time step Δt , as it should only ensure the Nyquist frequency $1/\Delta t$ is much larger than the FWHM of each distinct band not the total gain spectrum of a QD medium.

Take GS for example; substitute Eq. (2.35) in Eqs. (2.38) and (2.39), the frequency domain distribution of the gain and the refractive index changes can be rewritten as:

$$\begin{aligned} g_{GS}(\Omega) &= g_{GS}(\omega - \omega_{GS}) \\ &= g_{0,GS} \cdot \left(2\tilde{f}_{GS}(z, t) - 1 \right) \frac{\Gamma^2}{\Gamma^2 + (\omega - \omega_{GS})^2} \end{aligned} \quad (2.44)$$

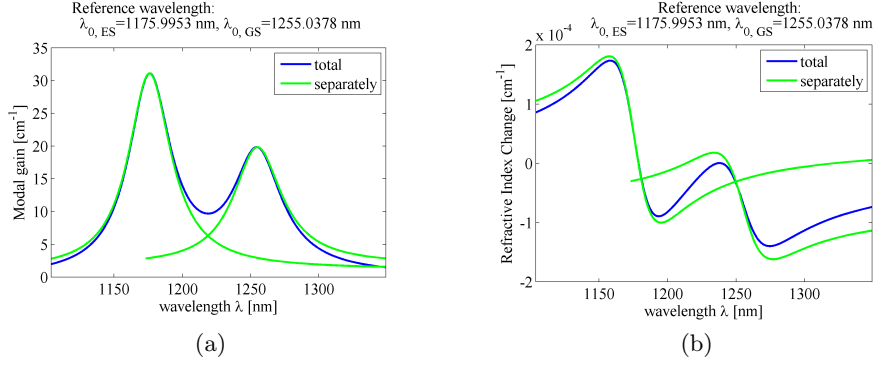


Figure 2.3: Simple schematic of the gain (a) and refractive index change (b) spectrum. The blue curves represent the total spectrum profile, while the green curves represent the profiles of these two parameters when we consider two distinct bands.

$$\begin{aligned} \Delta\eta_{GS}(\Omega) &= \Delta\eta_{GS}(\omega - \omega_{GS}) \\ &= \frac{c}{\omega_{GS}} g_{0,GS} \cdot \left(2\tilde{f}_k(z, t) - 1 \right) \frac{\Gamma(\omega - \omega_{GS})}{\Gamma^2 + (\omega - \omega_{GS})^2} \end{aligned} \quad (2.45)$$

As shown in Fig. 2.3, if consider the optical field with $\omega_0 = \omega_{GS}$, we obtain that $g_{GS}(\Omega = 0) = g_{0,GS} \cdot \left(2\tilde{f}_{GS}(z, t) - 1 \right)$ and $\Delta\eta_{GS}(0) = 0$. $g_{GS}(0)$ in time domain has the form as:

$$g_{GS}(t) = g_{0,GS} \cdot \left(2\tilde{f}_{GS}(z, t) - 1 \right) \Gamma \exp(-\Gamma t) \quad (2.46)$$

Whereas, if consider the influence of the GS field on the gain and refractive index change in the ES ($\omega = \omega_{ES}$), we can find that $g_{GS}(\omega_{ES} - \omega_{GS})$ is very small (neglected) and $\Delta\eta_{GS}(\omega_{ES} - \omega_{GS})$ can be written as:

$$\Delta\eta_{GS}(\omega_{ES} - \omega_{GS}) = -\frac{c}{\omega_{GS}} g_{0,GS} \cdot \left(2\tilde{f}_k(z, t) - 1 \right) \beta \quad (2.47)$$

where β is defined as:

$$\beta = \frac{\Gamma(\omega_{ES} - \omega_{GS})}{\Gamma^2 + (\omega_{ES} - \omega_{GS})^2} \quad (2.48)$$

Equation (2.47) represents the instant changes in the real part of ES the propagation constant, induced by the QD GS. This contribution is the main reason for the non-zero chirp in the ML pulses due to self-phase modulation [36]. Similar equations can also be derived for ES, when assuming $\omega_0 = \omega_{ES}$.

Time stepped solution of the travelling wave equation

To derive a proper finite-difference solution of the travelling wave equation Eq. (2.43), first we define a longitudinal discretization of the laser cavity with a unit step Δz , related with the simulation time step as $\Delta t = \frac{\Delta z}{v_{g,k}}$. Δz

should be small enough so that the dynamic changes of the field and the carriers are acceptable small when the pulse crosses each Δz . Since $v_{g,GS}$ dose not equal to $v_{g,ES}$, the corresponding simulation unit steps are also different, and $\Delta z_{GS} = v_{g,GS}\Delta t$ and $\Delta z_{ES} = v_{g,ES}\Delta t$ respectively.

Following the finite difference scheme in [24], we obtain the equation describing the cascade relation between the GS optical field at current slice $z_j \pm \Delta z$ and that at previous slice z_j :

$$\begin{aligned}
E_{GS}^{\pm}(z_j^{GS} \pm \Delta z_{GS}, t) &= J_{GS}^{\pm}(z_j, t)\Delta z_{GS} + E_{GS}^{\pm}(z_j^{GS}, t - \Delta t) \\
&- \frac{\alpha_i}{2} E_{GS}^{\pm}(z_j^{GS}, t - \Delta t)\Delta z_{GS} \\
&+ \Gamma_{xy}g_{0,GS} \left(2\tilde{f}_{GS}(z_j^{GS}, t - \Delta t) - 1 \right) I_{GS}^{\pm}(z_j^{GS}, t - \Delta t)\Delta z_{GS} \\
&+ j\beta\Gamma_{xy}g_{0,ES} \left(2\tilde{f}_{ES}(z_j^{GS}, t - \Delta t) - 1 \right) E_{GS}^{\pm}(z_j^{GS}, t - \Delta t)\Delta z_{GS}
\end{aligned} \tag{2.49}$$

$$\begin{aligned}
E_{ES}^{\pm}(z_i^{ES} \pm \Delta z_{ES}, t) &= J_{ES}^{\pm}(z_i, t)\Delta z_{ES} + E_{ES}^{\pm}(z_i^{ES}, t - \Delta t) \\
&- \frac{\alpha_i}{2} E_{ES}^{\pm}(z_i^{ES}, t - \Delta t)\Delta z_{ES} \\
&+ \Gamma_{xy}g_{0,ES} \left(2\tilde{f}_{ES}(z_i^{ES}, t - \Delta t) - 1 \right) I_{ES}^{\pm}(z_i^{ES}, t - \Delta t)\Delta z_{ES} \\
&- j\beta\Gamma_{xy}g_{0,GS} \left(2\tilde{f}_{GS}(z_i^{ES}, t - \Delta t) - 1 \right) E_{ES}^{\pm}(z_i^{ES}, t - \Delta t)\Delta z_{ES}
\end{aligned} \tag{2.50}$$

where we defined $I_k^{\pm}(z_j, t) = \mathcal{L}_k \otimes E^{\pm}(z_j, t)$, representing the forward and backward optical field filtered by the complex Lorentzian filters which describe the homogeneous broadened line-width of each considered interband transition (GS, ES). In the following, we use the notation for GS as an example to introduce the numerical model, but one should note that when calculating the quantities for the ES $k = ES$, we need to be use z_i .

Similarly, the finite difference solution for the filtered optical field at current slice can be calculated as ($k = GS$ or ES):

$$\begin{aligned}
I_k^{\pm}(z_j, t) &= e^{-\Gamma\Delta t} I_k^{\pm}(z_j, t - \Delta t) + \frac{1}{2}\Gamma\Delta t e^{-\Gamma\Delta t} E^{\pm}(z_j, t - \Delta t) \\
&+ \frac{1}{2}\Gamma\Delta t E^{\pm}(z_j, t)
\end{aligned} \tag{2.51}$$

Expression (2.46) is used in order to obtain Eq. (2.51). It actually corresponds to the implementation of a simple Infinite Impulse Response (IIR) numerical filter. Based on above considerations, the stimulated emission rate Eq. (2.41) appearing in the rate equation system Eqs. (2.15)-(2.16) can be simply written as ($k = GS$ or ES):

$$\begin{aligned}
R_{st,k}(z_j, t) &= \frac{\Gamma_{xy}}{\hbar\omega_0} g_{0,k} \left(2\tilde{f}_k(z_j, t) - 1 \right) \cdot \\
&\text{Re} \left\{ E^+(z_j, t) I_k^{+,*}(z_j, t) + E^-(z_j, t) I_k^{-,*}(z_j, t) \right\}
\end{aligned} \tag{2.52}$$

Numerical modeling of spontaneous emission noise

A similar procedure can be used to numerically calculate the spontaneous emission noise source $J_k^\pm(z_j, t)\Delta z_k$ appearing in Eqs. (2.49) and (2.50). The random spontaneous emission fields generated in different slices are required to be completely independent and have a power spectral density given by Eq. (2.42). These requests can be achieved by considering a set of independent random processes $\varphi_k^\pm(z_j, t)$, corresponding to the spontaneous emission in each longitudinal slice of the cavity. In addition, $\exp(j\varphi_k^\pm(z_j, t))$ has zero mean and unit mean square value.

In order to obtain the correct power spectral density, the random processes $\exp(j\varphi_k^\pm(z_j, t))$ are also filtered by the complex Lorentzian filter \mathcal{L}_k :

$$J_k^\pm(z_j, t)\Delta z_k = \sqrt{\frac{\beta_{sp}\hbar\omega_0 v_{g,k} n_k(z_j, t)}{2\pi\Gamma\tau_{sp,k}}} I_{sp,k}^\pm(z_j, t) \quad (2.53)$$

where $I_{sp,k}^\pm(z_j, t) = \mathcal{L}_k \otimes \exp(j\varphi_k^\pm(z_j, t))$ can be calculated via the approach analogous to obtain the Eq. (2.51):

$$I_{sp,k}^\pm(z_j, t) = e^{-\Gamma\Delta t} \left(I_{sp,k}^\pm(z_j, t - \Delta t) + \frac{1}{2}\Gamma\Delta t e^{j\varphi_k^\pm(z_j, t - \Delta t)} \right) + \frac{1}{2}\Gamma\Delta t e^{j\varphi_k^\pm(z_j, t)} \quad (2.54)$$

Numerical model implementation

Up to here, we presented a complete set of numerical solutions for the electromagnetic field, the polarisation and the spontaneous emission noise terms. To solve them numerically, we have to first discretize properly the time axis with unit step Δt and the laser cavity in its longitudinal direction (z-axis) with unit step Δz .

However, one may note that we include different group velocities for the GS and ES fields in the travelling wave equation Eq. (2.43). Therefore, for a given time step Δt , the corresponding unit steps for the GS and ES travelling wave equations are $\Delta z_{GS} = v_{g,GS}\Delta t$ and $\Delta z_{ES} = v_{g,ES}\Delta t$, respectively. Furthermore, the spatial grids for these two states have different total numbers that $N_{ES} > N_{GS}$ since $v_{g,GS} > v_{g,ES}$, which means that Eqs. (2.49) and (2.50) for GS and ES actually are calculated at different spatial grids $\{z_j^{GS}\}$ and $\{z_i^{ES}\}$. On the contrary, these two equations are coupled with each other through the rate equation system and therefore needed to be solved at the same longitudinal slice of the device. To overcome this problem, we consider the more dense grid $\{z_i^{ES}\}$ to solve the rate equations in each longitudinal section of the cavity and to calculate the spatio-temporal distribution of the occupation probabilities in the QD states $\tilde{f}_k(z_i^{ES})$ and

$\tilde{f}_k(z_i^{GS})$, which appear in the ES field equation Eq. (2.50). While the occupation probability distributions in the GS field equation Eq. (2.49) must be evaluated on a different spatial grid $\{z_j^{GS}\}$. To compute $\tilde{f}(z_j^{GS}, t)$ at the z_j^{GS} point, we therefore consider an average over the occupation probability values computed from the rate equations in the 2 nearest neighbouring slices belonging to the ES grid $\{z_i^{ES}\}$.

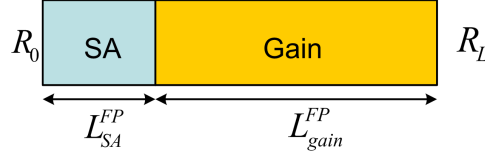


Figure 2.4: Simple schematic of a typical two-section passively ML FP laser. Forward biased gain section (yellow) and the reverse biased saturable absorber (light blue) are highlighted. R_0 and R_L stand for the reflectivities at the saturable absorber and the gain section side facets respectively.

As shown in Fig. 2.4, a typical two-section passively ML Fabry-Perot laser consists of a forward biased gain section and a reverse biased saturable absorber section. In our model, each longitudinal slice of the cavity can be assumed either forward or reverse biased, representing respectively the electrically isolated gain sections or saturable absorbers. The slice ensembles together with the reflectivity boundary conditions at two end facets establish a complete FB cavity.

Once the device structure has been defined, all the model variables are initialized. Then at each time step, the following procedures are performed, and iteratively repeated over the whole simulation time span:

- The rate equation system Eqs. (2.12) to (2.16) are solved in every longitudinal slice $\{z_i^{ES}\}$ to obtain the occupation probabilities in the QD states at the current time instant t ;
- The filtered optical terms $I_k^\pm(t)$ and $I_{sp,k}^\pm(t)$ at the current time instant t are evaluated for the GS and the ES at different grids $\{z_j^{GS}\}$ and $\{z_i^{ES}\}$ respectively from Eqs. (2.51) and (2.54);
- The corresponding spontaneous emission noise generated in each slice z_j or z_i are computed according to Eq. (2.53);
- The forward and backward travelling fields shift one step further in the cavity according to Eqs. (2.49) or (2.50) and the boundary conditions Eq. (2.11).

Note that in each iteration the variables for GS are calculated according to our previous description.

In this section, we explained the numerical scheme to solve the mathematical equations presented in previous three sections, which represents a complete model for simulation of the dynamics of the optical field and the carriers in a QD-based laser. Especially, we take into consideration the group velocity differences between GS and ES fields, so that devices involving optical emissions from both these two transitions can be simulated. However, to do so, the computational cost is relatively high. In principle, if the total static losses of one laser is not very high and can be satisfied by the gain from GS at a moderate injection current, there will be no stimulated emission from the ES transition and only GS emission can be observed. In this case, we can safely reduce the computational cost of this model by assuming $v_{g,ES} = v_{g,GS}$ and $E_{ES}^{\pm} = 0$. In this way, only the optical field from GS transition is fully simulated with a significantly reduced computational time. But even exploiting this approximation, the total simulation time using FDTW model still increases with the total length of the device, since the spatial discretization number N_{GS} is controlled by the simulation step $N_{GS} = L/\Delta z_{GS} = L/\Delta t v_{g,GS}$ which should be small enough to ensure validity of previous slowly varying approximation and to obey the Nyquist sample theorem. Thus, the investigation of long cavity devices using this model is still quite time consuming. In next section, a dual-state DDE model will be introduced which has a significantly reduced computational cost that is cavity length independent.

2.5 Multi-section dual-state DDE model

The alternative simplified DDE model started from the generalization of the analytical models from New and Haus [52], [53]. The standard DDE model was originally developed by Vladimirov *et al.* in [54] and [55] for the analysis of QD ML lasers. By assuming a unidirectional ring cavity, one can derive from the travelling wave equation an alternative set of equations to describe the field and carrier dynamics in the lasers. This equation set based on a novel delayed differential equation and a rate equation system. Unlike the FDTW model which can be easily applied to lasers with both unidirectional ring cavity and FP cavity, this model is originally valid only for former case. Nevertheless, qualitative agreement between DDE and FDTW models when performing the simulation of FP QD lasers has also been demonstrated (see [56], [57]).

Optical field dynamics

To do the simulations of a FP cavity ML laser using the DDE model, an equivalent unidirectional ring cavity is assumed with the total length being twice of the length for the FP cavity $L^{\text{Ring}} = 2L^{\text{FP}}$, as shown in Fig. 2.5a. Similarly, length of the gain and the SA sections for this ring cavity should

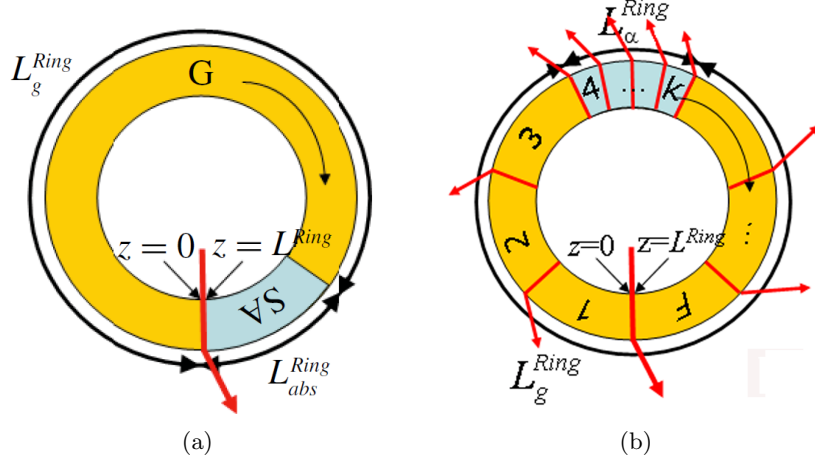


Figure 2.5: Simple schematic of the equivalent unidirectional ring laser described by the standard DDE model (a) and the MS-DDE model (b). Forward biased gain section (yellow) and the reverse biased saturable absorber (light blue) are highlighted. The simulated device consists of F isolated sections; red lines/arrows indicate the non-saturable losses introduced at each interface between adjacent sections (from reference [58]).

be $L_{\text{gain}}^{\text{Ring}} = 2L_{\text{gain}}^{\text{FP}}$ and $L_{\text{SA}}^{\text{Ring}} = 2L_{\text{SA}}^{\text{FP}}$. With respect to the TDTW model [59], the DDE model has several distinguished advantages in terms of computational cost and simplicity allowing therefore large parametric analysis of ML lasers. However, the fundamental underlying hypotheses, which enable its high efficiency, also reduce in part its accuracy. In the standard DDE model [54], a reference framework moving at the same group velocity of the pulse is assumed, by considering the following coordinate change from (t, z) to $(\tau = t - z/v_g, z)$. With this assumption, the complex field dynamics in the laser cavity can be simply represented just by the field at the reference section $z = 0$ and the slowly varying field envelope $E(\tau)$ in the reference section is governed by the following equation:

$$\frac{dE(\tau)}{d\tau} = -\Gamma E(\tau) + \Gamma R(\tau - T)E(\tau - T) \quad (2.55)$$

where T is the cold cavity round trip time given by $T = L^{\text{Ring}}/v_g$ with v_g the group velocity in the waveguide and L^{Ring} the equivalent unidirectional ring cavity length, Γ is the width of a Lorentzian function representing the spectral filtering effect in the laser cavity due to the finite gain spectral bandwidth and $R(\tau)$ represents the round trip gain or losses experienced by the field within the cavity.

Equation (2.55) can be directly derived from the travelling wave equations Eqs. (2.49) and (2.50) by introducing several suitable approximations. The detail derivation of it can be found in [54].

However, using this approach, all the distributed mechanisms such as the modal gain, the intrinsic losses, and the filtering effect due to finite gain spectrum bandwidth are modeled as lumped elements, limiting the accuracy of this model.

In order to improve the agreement between the DDE and the FDTW model, a multi-section DDE (MS-DDE) model has been proposed in [58], partially overcomes the problems in the standard DDE model by considering the laser cavity composed by an arbitrary number F of electrically isolated sections. A schematic of the proposed structure is shown in Fig. 2.5b. In this way, the modal gain and the unsaturable losses (the intrinsic losses) are considered distributed in a certain sense. As being compared in detail with the results from TDTW in [58], this MS-DDE model allows reliable and more quantitative description of the QD ML laser with respect to the standard DDE model and its low computational demand is preserved at the same time. However, in this model, it is assumed that the GS and ES field have the same group velocity, so the pulses from these two states are propagating with the same speed.

In this thesis, in order to take into account the desynchronization of ES and GS pulses due to their different group velocities, we approximate it as a lumped effect at the reference section $z = 0$. Thus, in this improved version of the MS-DDE, two delayed differential equations with different delay times are exploited, governing the time-domain evolution of the field envelope of GS and ES respectively:

$$\frac{dE_{GS}(\tau)}{d\tau} = -\Gamma E_{GS}(\tau) + \Gamma R(\tau - T_{GS})E_{GS}(\tau - T_{GS}) \quad (2.56a)$$

$$\frac{dE_{ES}(\tau)}{d\tau} = -\Gamma E_{ES}(\tau) + \Gamma R(\tau - T_{ES})E_{ES}(\tau - T_{ES}) \quad (2.56b)$$

where parameters have the same meanings as in Eq. (2.55) and the additional subscripts are used to distinguish the corresponding confined QD state.

Above two equations govern the evolution of the optical fields from GS and ES transitions. The basic property of all the DDE model is that we consider a reference framework moving with the pulse after doing the coordinate change from (t, z) to $(\tau = t - z/v_{g,k}, z)$. Therefore, $E(\tau)$ actually means the field amplitude of each point on the pulse and $R(\tau)$ is the round trip gain for the optical field at that point. To explain the physical meaning of Eq. (2.56), we rewrite it as:

$$E_k(\tau) = (\Gamma \exp(-\Gamma\tau)) \otimes (R_k(\tau - T_k)E_k(\tau - T_k)) \quad (2.57)$$

From this equation, we can immediately find that the first right-hand-side term is the time domain form of a Lorentzian function (see Eq. (2.35)).

So Eq. (2.57) means that the ML pulse crossing the reference section ($z = 0$) at a certain time $E_k(\tau)$ should equal to the pulse crossing the same section at one round trip time before $E_k(\tau - T_k)$ modified by the gain $R_k(\tau - T_k)$ and the spectral filtering effect $\Gamma \exp(-\Gamma\tau)$ it experienced during in this round trip. After one complete round trip within the cavity, based on Haus's analytic derivation [53], the criteria to establish a stable ML in absence of spectral filtering is that $R_k(\tau - T_k) = 1$ when $E_k(\tau - T_k) \neq 0$ whereas $R_k(\tau - T_k) < 1$ when $E_k(\tau - T_k) = 0$.

Being F the number of the electrically isolated sections in the laser cavity and L_m the length of the m^{th} section, the total ring cavity length is $L_{Ring} = \sum_{m=1}^F L_m$ and the cold round trip time for these two optical fields are calculated as $T_k = L_{Ring}/v_{g,k}$ ($k = GS, ES$).

To calculate the optical field profile at current time instant, the gain experienced by the pulse at previous round trip in the cavity $R_k(\tau - T_k)$ is therefore needed. This term can be computed as:

$$R_k(\tau - T_k) = \prod_{m=1}^F B_{k,m}(\tau - T_k) M_m; \quad (2.58)$$

where $B_{k,m}$ describe the gain experienced by the field at GS or ES transition when travelling across the m^{th} section and M_m describes the non saturable losses introduced at the interface between the m^{th} and $(m+1)^{\text{th}}$ section.

The term $B_{k,m}$ includes both the amplification/attenuation and the phase changes, which is time dependant. It can be written as:

$$B_{GS,m}(\tau - T_{GS}) = \exp(\Gamma_{xy} \bar{g}_{GS,m}(\tau - T_{GS}) L_m) \exp(j\beta \Gamma_{xy} \bar{g}_{ES,m}(\tau - T_{GS}) L_m) \quad (2.59)$$

$$B_{ES,m}(\tau - T_{ES}) = \exp(\Gamma_{xy} \bar{g}_{ES,m}(\tau - T_{ES}) L_m) \exp(-j\beta \Gamma_{xy} \bar{g}_{GS,m}(\tau - T_{ES}) L_m) \quad (2.60)$$

where β as already defined in 2.4, represents the changes in the real part of the propagation constant, induced by the ES field at the GS and vice versa.

Since we discretize the whole device to only few sections (F usually is not very large), $\bar{g}_{k,m}(\tau)$ actually is the averaged gain/absorption for the GS or ES in the m^{th} section. And can be calculated as $\bar{g}_{k,m}(\tau) = g_{0,k}(2\bar{f}_{k,m} - 1)$ with $\bar{f}_{k,m}$ is the occupation probability averaged over the m^{th} section.

While the term M_m includes intrinsic waveguide losses experienced by the field when travelling across the m^{th} section and power extraction losses $\sqrt{K_m}$ localized at two end facets (the reflectivity). This term is a time independent quantity at each interface between adjacent sections:

$$M_m = \sqrt{K_m} \exp\left(-\frac{\alpha_i}{2} L_m\right); \quad (2.61)$$

When considering a FP cavity ML laser, the total discretization number F should be even, and M_m should be chosen as:

$$M_m = \begin{cases} \sqrt{R_L} \exp\left(-\frac{\alpha_i}{2} L_F\right) & \text{if } m = F \\ \sqrt{R_0} \exp\left(-\frac{\alpha_i}{2} L_{F/2}\right) & \text{if } m = \frac{F}{2} \\ \exp\left(-\frac{\alpha_i}{2} L_m\right) & \text{if } m \neq F \text{ and } m \neq \frac{F}{2} \end{cases} \quad (2.62)$$

To solve the above equations numerically, there should be four vectors in the program which store GS/ES gain and optical field data within a entire round trip time, since for example in Eq. (2.56) both the field at current time instant and the field at one round trip time before are needed. Originally, the vector for GS gain should have a length of only $N_{GS} = T_{GS}/\Delta t$ which is smaller than N_{ES} , being Δt the simulation time step. However, as we have described in Section 2.4, the refractive index changes in the ES are mainly induced by the polarisation of GS through the parameter β . Therefore, consistently with what shown in Eq. (2.60), the GS gain value upto one ES round trip time T_{ES} ($T_{ES} > T_{GS}$) before should be stored. So the GS gain vector actually have the same length as that for the ES gain vector. Under this condition, in order to preserve correct round trip period for GS pulse circulating within the cavity, in the program, we consider two indexes for the GS gain vector, which rotate in the vector with different speeds $v_{g,GS}$ and $v_{g,ES}$, and therefore identify the location of $g_{GS}(\tau - T_{GS})$ and $g_{GS}(\tau - T_{ES})$ respectively.

Since we calculate the optical field at the reference section when $z = 0$, therefore $\tau = t - 0/v_{g,k} = t$. Then the numerical solution of Eq. (2.56) can be written as:

$$E_k(t) = E_k(t - \Delta t) + \Delta t \cdot \frac{dE_k(\tau)}{dt} + \Gamma \sqrt{\beta_{sp}} \Delta t \cdot e^{j\phi_k} \quad (2.63)$$

where the last term takes into account the spontaneous emission contributions.

Carrier dynamics

The temporal dynamics of $\bar{f}_{k,m}$ in each section of the ring cavity is calculated using the associated rate-equation system, which describes the carrier distribution dynamics in the QD medium. Due to the inherent hypothesis behind the DDE approach, $\bar{f}_{GS,m}$ and $\bar{f}_{ES,m}$ are computed assuming that the two fields are propagating with the same group velocity of the ES $v_{g,ES}$, within the cavity. The relative delay between these two fields, being T_{GS} different from T_{ES} , is introduced only as a lumped element at the reference section $z = 0$ to describe the field desynchronization. This approximation is possible because the difference between T_{GS} and T_{ES} is indeed less than 1 ps, so comparable with the typical QD carrier relaxation time in the sub-picosecond range [60], [61] and much shorter than the carrier radiative

or non-radiative recombination time (hundreds ps to several nanoseconds). The values of these parameters will be shown in following chapter when we discuss the real device performances.

Above mentioned rate equation system is almost identical to the one used in the TDTW model and described in Section 2.2 apart from the stimulated emission term. In this modified MS-DDE model, the stimulated emission rate at current time instant is instead calculated as:

$$R_{k,m}^{stim}(\tau) = (|B_{k,m}(\tau)|^2 - 1) \left(\prod_{n=1}^{m-1} |B_{k,n}(\tau)|^2 M_n^2 \right) \frac{|E_k(\tau)|^2}{\hbar\omega_k L_m}; \quad (2.64)$$

Physical meaning of above equation can be interpreted as that the total power lost at time τ in the active medium due to the stimulated emission recombination from state k in the m^{th} section $\hbar\omega_k R_{k,m}^{stim} L_m$ can be simply calculated as the difference between the instantaneous power coming out from the considered m^{th} section $\prod_{n=1}^m |B_{k,n}(\tau)|^2 M_n^2 |E_k(\tau)|^2$ and the instantaneous power going into the m^{th} section $\prod_{n=1}^{m-1} |B_{k,n}(\tau)|^2 M_n^2 |E_k(\tau)|^2$.

Output power

The output power from the reference section $z = 0$, is calculated as:

$$P_k^{out}(\tau) = \frac{1 - M_F}{M_F} |E_k(\tau)|^2 \quad (2.65)$$

Up to now, we present a complete equation set Eqs. (2.56) - (2.65) describing the temporal evolution of the field $E_k(\tau)$ in the reference section $z = 0$.

As been demonstrated in [58], quantitative agreement between the simulation results obtained from the FDTW model and the DDE model can be achieved starting from rather small spatio discretization number F . In the following, with this modified MS-DDE model, we chose to use $F = 28$ for the whole ring cavity consisting of 20 gain sections and 8 saturable absorber sections. This number is significantly smaller than the spatio discretization number for the same device using FDTW model, putting in evident that the MS-DDE model is much less time consuming for intense parametric investigation. However, since we consider a unidirectional ring cavity, the self-colliding effect happening close to two end facets is absent in this model. This effect indicates that the pulse interacts with itself in the SA and gain sections due to the coupling between the forward and backward propagating fields within the FP cavity. Therefore, in the investigation where this effect is dominant or crucial, we should employ the FDTW model.

2.6 Conclusion

In this chapter, theoretical equations governing the electromagnetic field propagation, the carrier population and the coupling between above two effects for the QD-based semiconductor lasers have been reported. In order to solve these equations numerically, two models, the FDTW and the revised MS-DDE, have been introduced. In both model, we paid special attention to include the group velocity differences between the optical fields at GS and ES wavelengths, so that the optical fields desynchronization and other related properties happening in the QD lasers involving emission from both QD states can be reliably simulated.

Although in this thesis these two models are mainly used to simulate the QD two-section passively ML lasers in Chapter3, they can be easily generalized and applied to lasers where not the mode locked pulse but the continuous wave (CW) emission happens. Furthermore, they can also be modified to simulate dynamics in the single-passing devices such as the semiconductor optical amplifier when an optical pulse passing through.

In addition, the steady state simulation results of the rate equation system described in Section 2.2 will be used as a input to the beam propagation method (BPM) model in Chapter 4 to simulate the properties of an optical beam propagating in a SOA. With the help of the results from the rate equation system, the gain saturation effect which has been experimentally observed in high power SOAs can be involved in the standard BPM model in a rigorous way.

Chapter 3

Passively mode locked QD lasers

Exploiting the FDTW and the revised MS-DDE models, the InAs/InGaAs QD-based FP passively ML lasers emitting around $1.3 \mu m$ are systematically investigated in this chapter. This particular class of the monolithic QD lasers allows the generation of short pulses separated with equal temporal space, i.e., with well defined repetition frequency which in principle equals to the round trip rate of the pulse within the cavity. The first demonstration of mode locking pulse generation using InAs/InGaAs QD material was in 2001 by Huang *et al.* [62]. Since then, intensely experimental investigations have been performed in this kind of devices in order to achieve better ML properties. Due to the inherent advantages of the QD semiconductor medium that has been introduced in Chapter 1, QD passively ML lasers are expected to achieve better performances in some aspects with respect to the QW or the bulk ML lasers. Up to now, experimental results have demonstrated high quality pulses with repetition frequency from few hundreds of MHz to hundreds of GHz [63], [64], pulse width ranging from tens of picosecond to hundreds of femtosecond [65], [66], [67], and peak power in the Watt range [65], [66], [68].

Good performances and together with the compact size and the high possibility to be integrated promote the potential usage of QD passively ML lasers in a large range of applications. In terms of telecommunications, they can be used as a stable optical pulse source generator for optical time division multiplexing and all optical clock recovery. In terms of analogue microwave optoelectronics, they are considered as stable microwave carrier generator or microwave optoelectronic frequency conversion component [69]. They can also be used in bio-medical applications such as cutting-edge biomedical imaging (nonlinear microscopy) [70] or in optical sampling and measurement.

To satisfy the high demands coming from these various applications,

further optimization and exploration of this passively ML QD-based lasers are still essential. As a matter of fact, from the experiment point of view, generally, only the pulse average power, the pulse width deconvoluted from autocorrelation pulse envelope, the radio-frequency (RF) spectrum and the optical spectrum can be easily obtained by measuring the pulse train outputting from the ML laser. Many other detail information of the pulse which are fundamental to study the complex pulse formation mechanisms, such as the temporal evolution of the output pulse train, the pulse energy distribution inside the laser cavity, the gain or absorption dynamics in the gain section or the SA, are not easy or even not possible to be directly measured. On the contrary, the theoretical numerical model considering approximately all the essential physical mechanisms in the QD ML lasers give us the possibility to gain insight of the ML system and the underlying pulse operation details.

Our activities were performed within the framework of the EU Seventh Framework Program "Fast Dot" Project. In the work presented in this chapter, we focus mainly on the possibility to optimize the GS ML performances of a passively ML QD laser. To this end, different laser configurations and even simultaneous GS and ES MLs were studied and the design strategy for device performance improvement was extracted. During these investigations, we always concentrated to study of the dynamics of the optical field inside the laser cavity and the related influences on the gain and the absorption. We obtained many interesting findings from this kind of simulations, which not only help us to learn and understand the passive ML processes in QD-based edge emitting lasers, but also supply very useful input to other groups within the FAST-DOT project for the device design and the experimental results interpretation.

Before showing the simulation results, a fundamental introduction of the passively mode-locking technique in the QD-based FP lasers is reported in Section 3.1. The theory there describes how the stable ML can be established in a two-section laser and how to make this achievement easier.

Then, in Section 3.2, properties of the QD medium, which are especially beneficial for the ML establishment, are stated. These properties generally indicate that the requests for a laser to achieve stable passive ML are well satisfied by the QD medium, therefore confirming that the QD-based lasers are very promising candidates for high power short pulse generations.

Various methods are introduced in this chapter for ML performance improvement. First in section 3.3, investigations of ML lasers exploiting only the GS emission are presented. It is well know that the S parameter plays an important role in indicating the ML stability and performances. In this section, ML improvements by varying structural parameters to achieve a higher S value are discussed. In addition, we also show that devices with the same S value still can be optimized to generate pulses with shorter pulse width and higher peak power.

In section 3.4, a systematic investigation of the role of several structural parameters on the obtained pulse properties for straight ML lasers is depicted. Device structural parameters, such as the saturable absorber (SA) length, the total cavity length and the facet reflectivities, have been varied. The obtained results indicate a strict relation between the ML performances and the intracavity evolution of the forward/backward travelling ML pulse. Especially, we pay attention to the determinant influence of the intracavity pulse energy and the corresponding gain/absorption dynamics on the pulse width reductions. We demonstrate that shorter pulses can be achieved in devices with higher intra-SA pulse energy thanks to the stronger absorption saturation.

Using the modified version of the multi-section delayed differential equation model, sole GS, sole ES, and dual-state lasing and ML in passively mode-locked QD lasers have been studied and are reported in Section 3.5. The results were verified also with TDTW simulations and compared, when possible, with experimental results. These tests confirmed the reliability of the model. We found that, in two-section ML lasers, GS lasing and mode locking are always more easily established. For instance, GS lasing can be either self-starting or induced by the initial lasing from the higher energy ES. On the contrary, GS lasing tends to inhibit, to a certain extent, the onset of ES lasing, especially at low injection current and low reverse voltage. Moreover, ES shows less potential to achieve stable ML than GS. Based on these findings, we propose proper theoretical explanation of the achieved lasing and ML regimes in realized devices. Especially, we demonstrate a novel stable dual-state ML regime with remarkable enhanced pulse peak power and pulse width.

Finally, a conclusion is drawn in Section 3.6.

3.1 Introduction of passive ML

There are various methods for generating optical pulses, such as gain switching and mode-locking. Gain switching pulses are obtained by switching the optical laser diode on and off using an external electrical signal, therefore the achievable pulse width and pulse repetition time is restricted by the characteristic of this electrical signal. While in the mode-locking, pulses generation is achieved through the locking of the longitudinal modes of a laser diode by controlling an intracavity gain, loss or phase element. There are generally three different methods to mode lock a laser structure, the active mode-locking, the passive mode-locking and the hybrid mode-locking.

Comparing with other methods, passive mode-locking is the only one that does not require any electrical modulation and therefore is widely used in many lasers to generate short pulses. The standard configuration of this

kind of lasers consists of two sections, one is the forward biased gain section and another one is the reverse biased saturable absorber section. The latter section is an essential element for a passively ML laser where the longitudinal cavity modes are locked in phase, so leading to a short and equal spaced optical pulses train. The fundamental pulse train repetition frequency or the ML frequency is defined by the round-trip time of a pulse inside the FP cavity, $f_{ML} = c/(2\eta_0 L)$, being c the light velocity in the vacuum, η_0 the effective refractive index and L the laser cavity total length. In some cases, harmonic ML may be achieved, i.e., there are more than one pulse circulating inside the cavity, then $f_{ML} = Nc/(2\eta_0 L)$ where N is the order of the harmonic ML.

The general principles of the theory of mode-locking have been established by New [52] and Haus [71], [53], and extended to passive ML in semiconductor laser structures by Koumans [72]. Stable mode-locked pulses can be designed by studying the properties of each components of the ML system.

Pulse broadening and amplification in the gain section

In the forward biased gain section, continuous current injection leads to population inversion in the QD band structures and shifts the electron quasi-fermi level into the conduction band, which means there are very high density of excited electrons in the conduction band. These electrons are ready to combine with the holes in the valence band when stimulated by a photon and generate an additional identical photon at the same time, we call this process the simulated emission and use the optical gain to describe the ability to generate additional photons.

When an optical pulse goes into the gain section, the beginning of the pulse leading edge experiences an uninfluenced optical gain and the optical field is amplified. While when the middle part of the pulse enters the gain section, excited electrons in the conduction band are already partially consumed by previous optical field, therefore the middle part experiences lower optical gain and is less amplified. Then for the pulse trailing edge, depends on the gain recovery rate, the optical field may amplified by an already fully recovered high optical gain or a still saturated low optical gain. Entire effect of above processes is a broadening of the original pulse width and an increase in the pulse energy.

The gain section usually is characterized by two parameters: the gain saturation energy and the gain recovery rate. The former one $E_{k,\text{sat,gain}}$ indicates the sufficient pulse energy to lead to substantial gain saturation and can be defined as [72]:

$$E_{k,\text{sat,gain}} = \frac{\hbar\omega_k W_{\text{gain}} N_{\text{lay}} H_{\text{QD}}}{\Gamma_{xy,\text{gain}}(dg_k/dn)} \quad (3.1)$$

where $k = GS, ES$, n is the averaged carrier density in the entire DWELL layers, W_{gain} is the width of the active region in the gain section, $\Gamma_{xy,gain}$ is the field confinement factor in the gain section and g_k is the material gain calculated as $g_{0,GS} \cdot (2\tilde{f}_{GS} - 1)$. Term dg_k/dn is usually called as the differential gain.

Generally speaking, the rate of change of the material gain with the total carrier density, i.e., the differential gain dg_k/dn , decreases with the injection current increasing due to the limited density of available states. Especially for the QD semiconductor medium, the highly reduced density of state leads to a early onset of gain saturation, the dg_k/dn is already very low at moderate injection current.

The gain recovery rate are decided by two factors. One is the cascading relaxation rates of the electrons from the SCH states to the GS. Another one is the current injection level.

To summarize, the injection current level is an important parameter for the gain section which determines the gain dynamics in this section.

Pulse shortening and attenuation in the SA

In the reverse biased SA, the conduction band is originally not occupied by the electrons, and therefore the absorber is ready to absorb photons with proper energy. Similarly, the leading edge field of the optical pulse experience higher absorption, so the optical power is reduced. In addition, the optical field-induced carriers occupy the conduction band and the valence band, reducing the absorption ability of the SA. Therefore, the middle part of the optical pulse will feel a saturated optical absorption and of course is less attenuated with respect to the leading part. At the same time, the field-induced carriers are swept out from the QD confined states via the enhanced thermionic and tunneling escape mechanisms induced by the bias electric field. Depending on the speed of these mechanisms, the trailing edge optical field may encounter different level of saturated absorption. So finally, the optical pulse is shortened when it propagates in the SA section.

Similarly, the absorption saturation energy can be calculated as:

$$E_{k,sat,SA} = \frac{\hbar\omega_k W_{SA} N_{lay} H_{QD}}{\Gamma_{xy,SA} (d\alpha_k/dn)} \quad (3.2)$$

where $k = GS, ES$, W_{SA} is the width of the active region in the SA section, $\Gamma_{xy,SA}$ is the field confinement factor in the SA section and α_k is the material absorption calculated as $g_{0,GS} \cdot (1 - 2\tilde{f}_{GS})$. Term $d\alpha_k/dn$ is usually called as the differential absorption.

From Eqs. (2.28) and (2.27), we can see that the two main carrier sweep-out paths in the SA, i.e., the enhanced thermionic and tunneling escape mechanisms, are all related with the reverse bias voltage. Therefore, the absorption recovery rate is strongly influenced by that parameter.

Thus, the reverse voltage applied to the saturable absorber is determinant for the field and carrier dynamics happening in the SA. To establish a stable ML pulse train, this parameter should be properly controlled.

Self-phase modulation (SPM)

As described in Section 2.3, the optical response of a QD medium not only induces gain/absorption, but also leads to changes in the refractive index. Being respectively the imaginary and the real parts of the optical susceptibility, the gain/absorption and the refractive index are strongly coupled with each other according to the Kramers-Kronig relation [73]. As a result, the changes of the carrier density in the gain and SA sections are accompanied by large changes in the refractive index.

The non-linear changes in the refractive index in the gain and the SA sections will lead to corresponding variation in the instantaneous carrier frequency along the pulse envelope. This phenomenon is usually referred as the self-phase modulation, which leads to chirp in the ML pulses and may shorten or broaden the pulse by interacting with other dispersion mechanisms in the laser system, such as the gain and the group-velocity dispersions.

In principle, an ideal unchirped pulse with a Gaussian envelope should have a time-independent carrier frequency, which means that its optical spectrum has a constant phase over the whole wavelength band. In this case, we call this pulse as a transform limited pulse and the product of the FWHM of the pulse duration $\Delta\tau$ and the FWHM of the optical spectrum Δf would be a constant of about 0.44. While, in reality, the Gaussian pulse with the same pulse duration always has a instantaneous frequency chirp in the time domain, which is equivalent to a bandwidth broaden of the optical spectrum of this pulse, therefore the time bandwidth product (FBWP) of this pulse is increased with respect to an ideal unchirped pulse and $\Delta\tau \cdot \Delta f > 0.44$. Both the pulse duration and the optical spectrum bandwidth can be easily measured via standard experimental techniques. Therefore, this time bandwidth product $\Delta\tau \cdot \Delta f$ is usually considered as a standard and simple way to experimentally quantify the chirp of a ML pulse.

In Sections 2.3.1, 2.4 and 2.5 we introduced in detail how to include this mechanism in our numerical model. Indeed, the strong coupling between the changes in the optical gain/absorption and the refractive index is simply represented by the parameter β in the single-population FDTW and MS-DDE models.

In above paragraphs, we recalled the main mechanisms that govern the formation of a well-shaped pulse circulating in a two-section passively ML laser cavity consisting of a SA, a gain section.

The stable ML pulse train is actually a self-consistent solution of the complex ML system, which balances above described mechanisms in the gain and the SA sections and also the boundary condition at two end facets so that the shape and the energy of a pulse are exactly reproduced after one complete round trip within the laser cavity. Thanks to the efforts of New, Haus and Koumans, their analytic investigations already indicated few key conditions that needs to be satisfied by the laser system to achieve a stable ML regime. These analytic findings are still very useful when applied to the QD semiconductor lasers.

The stable parameter S

The so-called stability parameter S is defined as the ratio between the gain saturation energy and the absorption saturation energy. According to Eqs. (3.1) and (3.2), this parameter in the straight QD-based lasers can be calculated as:

$$S_k = \frac{E_{k,\text{sat,gain}}}{E_{k,\text{sat,SA}}} = \frac{W_{\text{gain}}\Gamma_{xy,SA}(d\alpha_k/dn)|_{n_k=0}}{W_{SA}\Gamma_{xy,\text{gain}}(dg_k/dn)|_{n_k=n_{p,th}}} \quad (3.3)$$

where $k = \text{ES}$ or GS , $E_{k,\text{sat,gain}}$ is the saturation energy for the gain section, $E_{k,\text{sat,SA}}$ is the saturation energy for the SA and $n_{p,th}$ is the averaged carrier density in the entire DWELL layers at the threshold current of a ML laser.

Above equation can be simplified to the ratio of the differential absorption and the differential gain when applied to the straight QD lasers where $W_{\text{gain}} = W_{SA}$ and $\Gamma_{xy,\text{gain}} = \Gamma_{xy,SA}$ as:

$$S_k = \frac{(d\alpha_k/dn)|_{n_k=0}}{(dg_k/dn)|_{n_k=n_{p,th}}} \quad (3.4)$$

One should note that in our numerical model using Eq. (3.3) or (3.4), the calculated S parameter actually corresponds to the case where the gain section forward injection current is the threshold current and the SA is reverse biased at 0 V. If we increase the injection current, differential gain will be reduced leading to higher gain saturation energy and larger S . On the contrary, if we increase the reverse voltage, due to enhanced thermionic and tunneling escape processes, differential absorption will decreases resulting to higher absorption saturation energy and smaller S .

In principle, the ML system should make sure that $S > 1$. Physically, this means the gain section is harder to be saturated than the absorber, so that initially the pulse narrowing achieved in the SA will not be fully compensated by the broadening processes in the gain section therefore leading to the formation of a short pulse. As the pulse peak power also increases associated to the pulse shortening, the final stable ML regime should have

a proper pulse width that balances the saturation in the gain and the SA sections.

According to the analytic investigations, another important advantages of a large value for the S parameter is that the bias condition range where stable mode-locking can be achieved becomes larger and that bias range moves toward the threshold condition [72]. These findings have been confirmed by our numerical simulations. It is always found that we gain larger stable ML area by modifying the laser configurations to reach a larger S value. In addition, although is not directly related with the ML performances, we also noticed that optimizing the S parameter would let us obtain shorter pulses with much higher peak power.

The round trip gain and absorption

In this part, we study the conditions of the gain/absorption dynamics for stable mode locking. To this end, we define a reference framework moving together with the pulse in the laser cavity by mapping the variables at (z, t) to $(z, \tau = t \mp \frac{z}{v_{g,k}})$ (the sign indicates whether the pulse is forward $+z$ or backward $-z$ propagating in the laser cavity), similarly to what we did in the numerical implement of the DDE model. In this way, τ corresponds to the location of each point on the ML pulse, and varying τ is equivalent to moving along the pulse envelope. With this transformation, the net gain experienced by each point of the pulse in a complete round trip in the laser cavity $R_k(\tau)$ can be simply calculated according to:

$$R_k(\tau) = \sqrt{R_0 R_L} \exp \left[\Gamma_{xy} \int_0^L (g_k^+(z, \tau) + g_k^-(z, \tau)) dz - \alpha_i L \right] \quad (3.5)$$

where $k = GS$ or ES , $g_k^\pm(z, \tau)$ are the material gain from GS and ES wavelengths experienced by the pulse when propagating in the direction $+z$ and $-z$ respectively.

For a passively ML laser with a gain section and a SA section, above net gain equation can be divided into two terms, one represents the averaged gain/amplification experienced by the pulse per unit length $G_k(\tau)$ and one represents the averaged losses/attenuation experienced by the pulse per unit length $A_k(\tau)$:

$$\frac{1}{L} \ln R_k(\tau) = G_k(\tau) - A_k(\tau) \quad (3.6)$$

where the averaged gain and losses (in cm^{-1}) can simply be computed as:

$$\begin{aligned}
G_k(\tau) &= \frac{\Gamma_{xy}}{L} \int_{L_{SA}}^L (g_k^+(z, \tau) + g_k^-(z, \tau)) dz \\
A_k(\tau) &= -\frac{\Gamma_{xy}}{L} \int_0^{L_{SA}} (g_k^+(z, \tau) + g_k^-(z, \tau)) dz + \alpha_i + \alpha_m
\end{aligned} \tag{3.7}$$

where L is the total cavity length of the laser, L_{SA} is the length of the SA section, and the last term for $A_k(\tau)$ is the mirror losses which takes in to account the optical power extraction losses from two end facets and can be defined as:

$$\alpha_m = \frac{1}{L} \ln \left(\frac{1}{\sqrt{R_0 R_L}} \right) \tag{3.8}$$

According to the analytically defined conditions [72], [52], [53], in order to avoid that perturbations preceding and following the pulse can grow, the net gain preceding and following the pulse must be negative, equivalent to $G_k(\tau) < A_k(\tau)$. In Fig. 3.1, we show an example of the net gain profile of a ML pulse which satisfies the stability criterion and the corresponding pulse envelope.

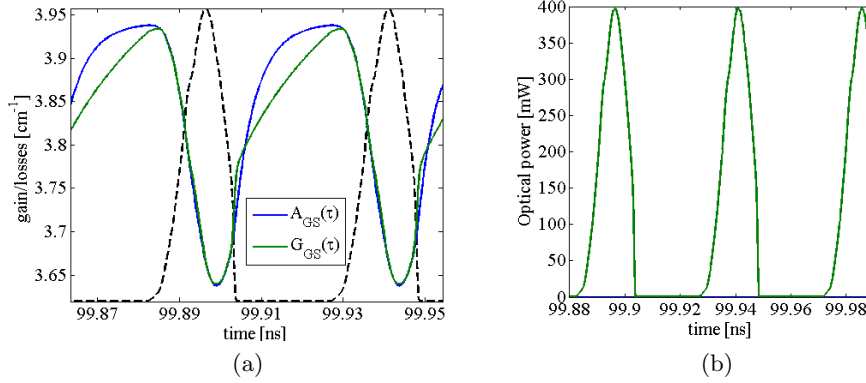


Figure 3.1: (a) Net gain profile of a stable ML pulse and (b) the corresponding pulse envelope.

We can see that at the time window where exists the pulse, the total gain equals the total losses, guaranteeing that an identical pulse can be reproduced after one successive round trip in the laser cavity. On the contrary, the averaged gain must be smaller than the averaged total losses at the swings of the pulse, so that the pulse is stable to noise perturbations before and after the pulse, since they are attenuated in each round trip. As a result, the obtained pulses are equally separated and identical in terms of the pulse energy and the shape.

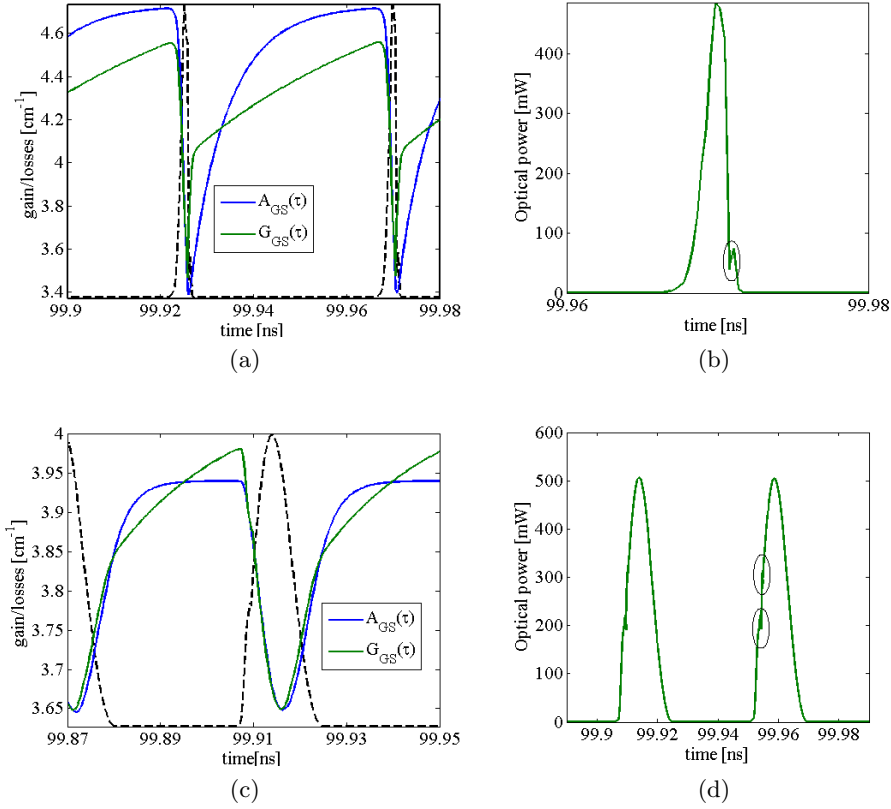


Figure 3.2: (a) Net gain profile of a ML pulse with trailing edge instability and (b) the corresponding pulse envelope; (c) Net gain profile of a ML pulse with leading edge instability and (d) the corresponding pulse envelope.

However, if above conditions can not be satisfied, time domain instability or even pulse collapse may happen, as shown in Fig. 3.2.

Originally, the pulse energy should be large enough to pull down the gain to a value below the loss after the passage of the pulse [72]. Otherwise, a positive net gain region will appear immediately after the pulse (Fig. 3.2a) and the spontaneous emission noise generated in this time interval may be amplified and leads to instability. This is commonly referred as the trailing edge instability (TEI). In the case shown in Fig. 3.2a, beside the insufficient pulse energy, the initial, ultrafast recovery of the averaged gain also attributes to the present of a positive net gain time interval after the pulse. This initial fast recovery stage actually relates both with the pulse energy and with the pulse width [74]. Under the TEI condition, the amplified spontaneous emission noise will show as small spikes at the trailing edge of the main pulse, as shown in Fig. 3.2b, leading to also large amplitude jitter of the pulse train. We found that the TEI always happens in the devices

with very high S value and generating ultra-short pulses, but fortunately, this problem can be solved by increasing the reverse bias voltage.

In addition, the pulse energy should not be too high so that there is not a positive net gain for the perturbations preceding the pulse. In principle, at the threshold current, the total unsaturated gain and loss are equal, while as increasing the injection current, the unsaturated gain will exceed the total unsaturated losses. Therefore, at current well above the threshold, if the averaged gain recovers completely between two succeeding pulses, the net gain would be positive at the leading edge of a pulse (Fig. 3.2c), and the spontaneous emission noise can be amplified within this net gain window generating amplitude jitter and pulse shape distortion of the ML pulses (Fig. 3.2d). This is the leading edge instability (LEI). If LEI is even stronger, the laser will finally work in the continuous wave regime.

In addition to above conditions, to establish a stable ML, the laser system should be self-starting. Generally, this condition can be achieved by adjusting the injection current up to a threshold value.

Through the descriptions in this section, we already revealed the complexity of a passively mode-locking laser and the conditions that need to be satisfied in order to generate stable short pulse train. As a promising candidate for future generation optical sources, the QD material exhibits advantages in many aspects that make above conditions easier to be satisfied and therefore especially benefit the generation of short pulses. In next section, these points are therefore introduced. Understanding them not only gains more insight of the ML mechanisms but also helps the design of QD-based ML lasers.

3.2 Special advantages of QD ML lasers

Comparing with the QW and bulk counterparts, QD medium as an active region material distinguishes itself mainly due to following potential advantages:

Large S parameter value

In above section, it has been pointed out that S larger than one should be guaranteed to format a pulse. And it will be much easier to establish pulse shaping if the gain is much harder to be saturated than the absorption.

According to Eq. (3.4), for the straight QD two-section ML lasers where the gain section and the SA section have uniform transversal section, the stability S parameter can be calculated as the ratio between the differential absorption and the differential gain. In addition, for semiconductor materials, the differential gain decreases when injection current and in turn the

carrier density increases due to the limited density of states. This fact ensures that the differential absorption is larger than the differential gain and the S parameter is larger than one. This effect is more pronounced in QD-based devices, due to the extremely reduced density of states as introduced in Section 1.2.

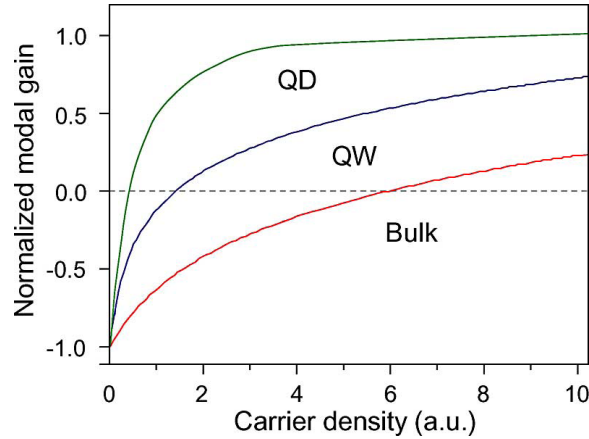


Figure 3.3: Simple schematic of the normalised modal gain as a function of the carrier density for the bulk, QW and QD materials. Figure from [11].

In Fig. 3.3, it is shown schematically the evolution of the modal gain for the bulk, QW and QD materials against the carrier density. Using Eq. (3.4), one can easily find that the S parameter is highest in the QD material, which indicates that this material system is more easily to establish stable ML. More precisely, the absorption saturation energy for a QD layer has been demonstrated to be 2-5 times smaller than a QW layer [46].

Broad gain spectrum

In Section 1.2, we have introduced the commonly used fabrication approach of QD, i.e., the self-assembled QDs, and the corresponding properties of QD ensembles obtained from this approach. We shown that due to the distributions of the QD size, shape and composition, significant inhomogeneous broadening of the gain/absorption spectrum exists in the QD medium. This effect may be detrimental for many applications, but it is really a good property for an active material that is intended to generate ML pulses. A broad gain bandwidth allows more longitudinal modes to be phase locked and therefore leads to ultra-short pulse even in sub-picosecond range.

In addition, the shape and size distributions of the QD ensembles can be controlled during the QD fabrication proceedings [18], [19] and [75], leading to associated changes in the laser emission spectrum. Therefore, the gain spectrum of the QD material can be easily adjusted.

Especially, using the chirped QD structure, i.e., the QD layers in the active region varies in terms of the composition so that each group of QD layers displays a different central emission wavelength [76], broad gain spectrum covers continuously from the GS wavelength (1283 nm) to the ES wavelength (1187 nm) has been demonstrated [77], [78]. This technique enables ultra-short pulse generation and the implement of large emission wavelength tunability in a single laser.

Fast gain/absorption recovery rate

Fast gain, especially fast absorption recovery rate are key factors that facilitate high speed applications of QD-based devices. For passively ML lasers, the absorption is expected to be fully recovered before the arrival of the next pulse.

Generally, increasing the reverse voltage leads to faster removal of the carriers from the absorber, thus increasing the absorption recovery speed. For the 1.3 μm InAs/InGaAs QD materials, ultra-fast absorption recovery with characteristic times of about 700 fs for a QD absorber under the reverse voltage of 10 V has been demonstrated from the pump-probe differential transmission experiments [46]. This fast recovery can be mainly attributed to the highly enhanced tunneling escape of the carriers which happens usually when applying very high reverse voltage to the absorber.

In addition, in the pump and probe experiments, ultra-fast gain recovery time in sub-picosecond range has been demonstrated in [61], [60] and [79]. Especially, in [79], the initial gain compression of GS (the spectral hole burning) recovers in only 100 fs, which should be attributed to the ultra-fast carrier relaxation from the higher ES to the GS.

Low noise

Noise inside the laser cavity causes instabilities in the mode-locking pulses, as we discussed before in Section 3.1. The amplitude and time jitters introduced by it are undesired properties for a ML laser. As pointed out in [80], the key method to improve the noise performance of a device is to reduce the pulse reshaping in the gain and absorber sections. It is well known that spontaneous emission is the main contribution of the noise generated in a device and it relates directly to the carrier density. Reducing the pulse reshaping could help to reduce the dynamic losses and the carrier density required to reach the threshold, therefore leading to improvement of the noise performances of a device. As described above, QD lasers have intrinsically high gain saturation energy, and therefore small pulse reshaping happening in the gain section, reducing the noise level in the cavity [11].

For the QD devices, due to the reduced density of state, ML operation relies on a relatively smaller threshold current if comparing to their QW and

bulk counterparts. As a result, the spontaneous emission arising from the QD active layers is smaller [81], [82]. Besides, QD ML lasers are attracting low noise sources also because they have lower intrinsic waveguide losses [83] and low linewidth enhancement factor [84], which ensure the good noise performances in this kind of device [85].

Low linewidth enhancement factor

The linewidth enhancement factor (LEF) (sometimes referred as the α -factor) describes the coupling relation between the optical gain and the refractive index changes, as the β we defined in Section 2.4. This parameter determines the bandwidth of the pulse optical spectrum and the instantaneous frequency chirp of the pulse and should be as small as possible at the gain peak. It has been demonstrated that the LEF is much smaller in the QD materials than that in the QWs [86], [87], implying that reduced wavelength chirp [84] and transform-limited ML pulses [65] are easier to be achieved in QD lasers. These experimental findings actually originate from the fact that the QDs gain spectrum is almost symmetric and thus the refractive index changes at the gain peak are negligible.

In this section, we reviewed the reasons why QD lasers are particularly interesting as optical pulse sources. Although the QD materials already supply a large range of inherent advantages to the engineer, designing a good QD-based ML laser that exploits properly above illustrated properties is much more difficult and important than just fabricating a QD-based waveguide wafer. Due to the discrete energy levels in the QD medium, the gain and absorption dynamics governing the pulse generation in a QD laser are more complex than that in the QW or bulk lasers. Full understanding of them will help us in a large amount to design a laser with appropriate configuration guaranteeing the stability of the ML system. In the following sections, comprehensive investigations of passively ML QD lasers in the purpose to optimize the ML performances and to get more insight of the underlying physical mechanisms in QD lasers will be shown.

3.3 GS ML performances improvement

We have discussed previously the role of the S parameter as a stable criteria for the ML system. However, this parameter can also be considered as a simple indicator for the ML performances, i.e., varying the laser configuration to increase the value of S in one ML laser could benefit the pulse width and the peak power of the pulses obtained from that laser.

In this section, we show firstly the various methods that can be used to push the laser to higher S value and the advantages and drawbacks of these methods in Subsection 3.3.1. Then, in Subsection 3.3.2, we demonstrate that for devices with the same S value, ML performances still have potential to

be improved. We focus only on the optical pulses from the GS transition in this section, therefore the label $k = GS$ is ignored in the following.

3.3.1 Lasers with higher value of the stability parameter S

According to Eq. (3.3), we introduce in the following different methods to push the S parameter for one device to higher level.

Change the length of the SA

From Eq. (3.4), we can see that for a straight ML laser if the reverse voltage and in turn the saturation energy are fixed, S value will relates directly to the differential gain. As described in Section 3.2, the differential gain decreases with the injection current density. Therefore, it is obvious that we can assume different straight lasers have the same S value if they have the same threshold current I_{th} or the same threshold gain g_{th} (of course, these lasers should have the same active material).

For the two-section FP cavity laser, g_{th} are estimated using the following approximate resonance equation [88]:

$$\frac{L - L_{SA}}{L} \Gamma_{xy} g_{th} = \frac{L_{SA}}{L} \Gamma_{xy} \alpha_{SA} + \alpha_i + \frac{1}{L} \ln \left(\frac{1}{\sqrt{R_0 R_L}} \right) \quad (3.9)$$

where α_{SA} is the QD unsaturated material absorption at GS transition. The last term in the right hand side of Eq. (3.9) represents the mirror losses α_m of the laser cavity.

One can easily find that increasing the SA length, which is equivalent to increase the cavity losses, would push the threshold gain to higher value and also the S parameter.

In [89], a multi-segmented QD laser with total length of 2 mm, mode-locking repetition rate of 20.5 GHz has been investigated. This multi-segmented approach allowed the device to be configured with SA length ranging from 65 to 650 μm by connecting different electrically isolated sections together. In this paper, a reduction of the pulse width from 2.3 ps to 800 fs, associated with five-fold increase in the average power and 14-fold increase in the peak power have been demonstrated when changing the gain-to-absorber section length ratio from 14:1 to 3:1.

Similarly, the trends of increases in the peak power and reductions in the pulse width by increasing L_{SA} have been confirmed theoretically in [74] via systematic simulations using the DDE model. However, it has also been shown in this paper that the devices with higher S value may suffer stronger trailing edge instability due to the enhanced initial ultra-fast gain recovery.

Use the tapered gain section

In this part, we consider index-guided QD ML lasers with non-uniform cross section. From Eq. (3.3), it is obvious that if the increase in the confinement factor Γ_{xy} is not linearly proportional to laser lateral width, then increase the width of the gain section could be a effective way to get higher S parameter. In order to avoid abrupt changes in the waveguide cross-section, the tapered configuration should be considered, where the lateral width of a section increases gradually. This configuration has already been widely exploited in the broad area lasers since it guarantees high power and good beam quality simultaneously [90]. When applying this technique to the QD ML lasers, significant increase of the peak power and corresponding significant decrease of the pulse width have been demonstrated both experimentally [65] and theoretically [74]. Our colleagues Nikitichev *et al.* from University of Dundee (UK) have achieved state of art pulse performances using this tapered gain section configuration [68]. In this part, we show that a proper tapered angle should be used to get optimum pulse performances.

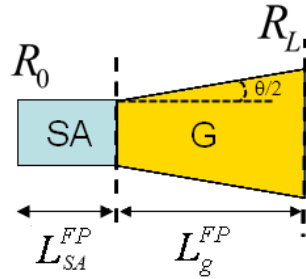


Figure 3.4: Schematic of a QD ML laser with tapered gain section (G) and reverse biased saturable absorber (SA).

To simulate a ML laser with non-uniform cross section, in principle, distributed time-domain models resolving the field dynamics in both the longitudinal and lateral directions of the laser cavity should be developed [91]. However, such model have an extremely high computational cost. In order to overcome this problem, we use a simplified but computational efficient method for the simulation and design of QD ML lasers with tapered gain sections. This method involves the use of the MS-DDE model (Section 2.5) where parameters describing the propagation along the non-uniform waveguide are extracted from preliminary simulations using a static finite-difference beam propagation method which will be introduced in detail in Chapter 4.

We consider tapered QD ML lasers with total length of 3 mm, SA length of $450 \mu\text{m}$, facet reflectivities $R_0 = 0.99$ and $R_L = 0.1$, and different full angles $\theta = 0^\circ, 0.3^\circ, 0.6^\circ, 1^\circ, 1.5^\circ$ characterizing the tapered section, as schemat-

ically shown in Fig. 3.4.

With respect to the MS-DDE model in Section 2.5, the non-uniform waveguide cross-section is included in the simulations by introducing sections $k = 1 \sim F$ with different values for W_k , $\Gamma_{xy,k}$ and $\alpha_{int,k}$ where the last two parameters are extracted from BPM simulations. In order to extract them for each section composing the equivalent ring laser in the DDE model, a finite-difference BPM is used, where waveguides as those depicted in Fig. 3.5, consisting of two replica of the tapered laser under study are investigated.

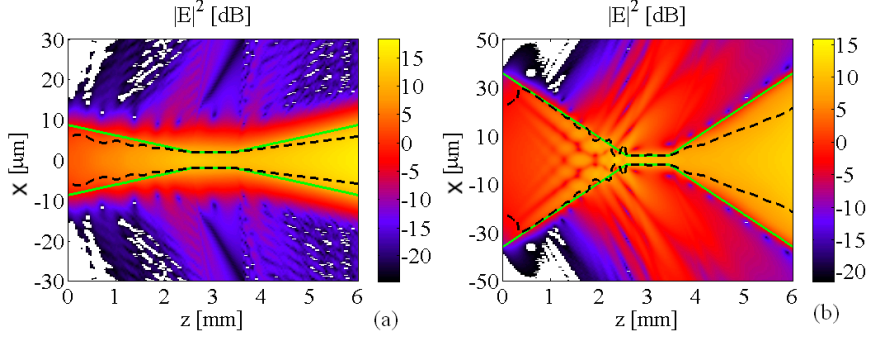


Figure 3.5: BPM simulation of the field profile evolution during forward and backward propagation across the tapered device with $\theta = 0.3^\circ$ (a) and $\theta = 1.5^\circ$ (b). Black dashed lines represent a reduction of -3 dB with respect to the maximum field intensity in each longitudinal section of the device. Continuous green lines represent the waveguide profile, $x = \pm W(z)/2$, being $W(z)$ the ridge width as a function of the longitudinal coordinate z .

For the entire waveguide, A step index $\Delta n = 3 \cdot 10^{-3}$ is considered to guarantee that a single transverse mode is guided within the straight SA section. The BPM procedure is performed iteratively until a self-consistent field distribution is achieved. Optical intensity distributions $|E|^2(x, z)$ for the devices with $\theta = 0.3^\circ$ and $\theta = 1.5^\circ$ are shown in Fig. 3.5a and Fig. 3.5b, respectively. For $\theta = 0.3^\circ$, the field transforms adiabatically along the tapered section, remaining well confined within the ridge; on the contrary for $\theta = 1.5^\circ$, radiation losses are clearly visible, reducing the overlap between the field profile and the SA transversal section.

From the calculated field distributions, values for $\Gamma_{xy,k}$ and $\alpha_{int,k}$ are computed. $\Gamma_{xy,k}$ is factorized in terms of the confinement factors along y and x directions: $\Gamma_{xy,k} = \Gamma_y \cdot \Gamma_{x,k}$. The confinement factor in the QD layers along the growth direction, Γ_y , is constant whereas $\Gamma_{x,k}$ is calculated as:

$$\Gamma_{x,k} = \frac{1}{L_k} \int_{z \in L_k} \left\{ \frac{\int_{-W(z)/2}^{+W(z)/2} |E|^2(x, z) dy}{\int_{-\infty}^{+\infty} |E|^2(x, z) dy} \right\} dz \quad (3.10)$$

Instead of the constant intrinsic losses α_i , now we model the unsaturable

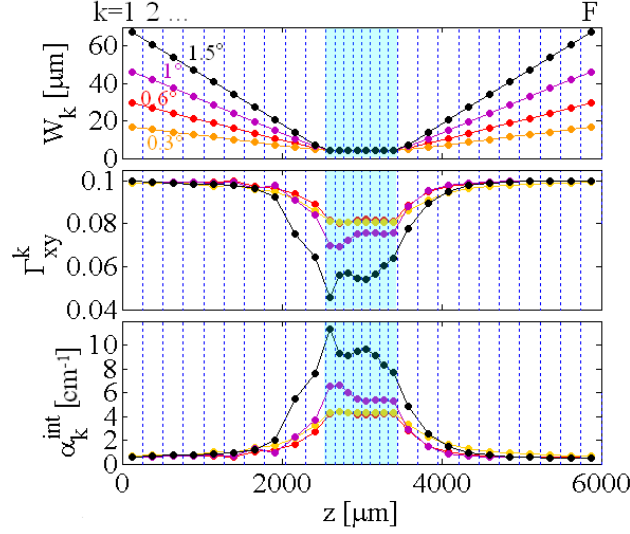


Figure 3.6: Ridge width W_k , field confinement factor $\Gamma_{xy,k}$ and internal losses $\alpha_{int,k}$ for tapered devices with $\theta = 0.3^\circ, 0.6^\circ, 1^\circ, 1.5^\circ$.

losses in the laser cavity using a internal loss term $\alpha_{int,k}$ which can be expressed as $\alpha_{int,k} = \alpha_i + \Gamma_y(1 - \Gamma_{x,k}) \cdot \alpha_{ext}$, where α_{ext} is the absorption outside the ridge and α_i is the additional losses due to doping and defects. The obtained values for $\Gamma_{xy,k}$, $\alpha_{int,k}$ are shown together with W_k in Fig. 3.6 for the different tapered lasers.

Based on the parameters obtained from the BPM simulations, the ML regimes in the devices under study are then simulated using the MS-DDE model. Fig. 3.7 shows maps of peak power and pulse width as a function of the applied gain current and SA reverse voltage for all the considered devices. For small tapered full angles ($\theta = 0^\circ, 0.3^\circ$), the maximum achievable average and peak power is limited by the onset of a large leading edge instability in the ML pulse train with increasing current, furthermore the pulse duration remains always larger than 1 ps. With increasing θ , the LEI tends to disappear even for current well above threshold whereas a TEI is found for moderate SA reverse voltages. Furthermore, at very large currents (large pulse energy), a pulse breakdown induced by the action of the large self-phase-modulation and dispersion is observed. With increasing θ , a significant pulse shortening is found so that for $0.6^\circ, 1^\circ$, ultra-short sub-picosecond pulses are achieved. Such a reduction in the pulse width is attributed to the further increase in the gain saturation energy and in turn the S parameter as we predicted above. The shortest pulse width and largest peak power are achieved at 1° . On the contrary increasing further the full angle (1.5°) no significant improvements in the ML regimes are obtained.

This is clearly due to the fact that for too wide tapered full angles, the

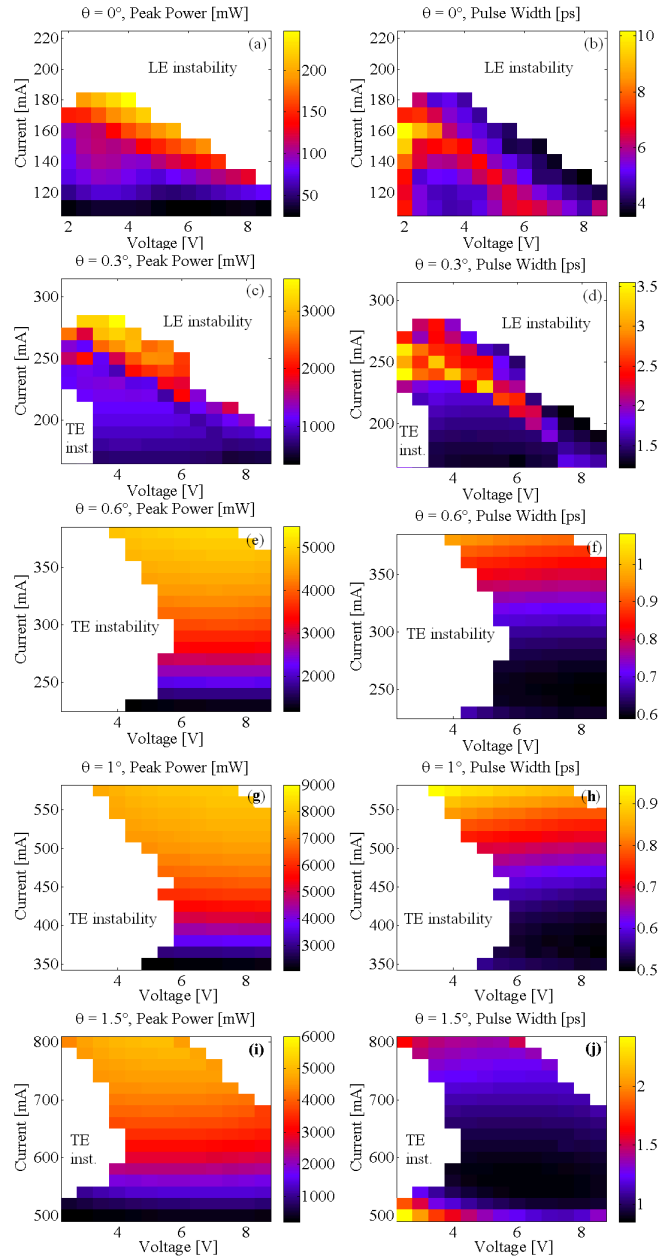


Figure 3.7: Maps of pulse peak power and pulse width as a function of the current applied to the gain section and voltage applied to the SA for devices with $\theta = 0^\circ$, 0.3° , 0.6° , 1° and 1.5° .

field profile does not transform adiabatically when travelling back across the tapered section and significant radiation of the field occurs (Fig. 3.5b); this leads to a large decrease in the overlap between the field profile and the reverse biased SA (Fig. 3.6), reducing therefore the effectiveness of the SA

in shaping the ML pulses.

Therefore, when designing the passively ML QD lasers with tapered gain section, a proper total taper angle should be chosen so that an adiabatic transformation of the field profile along the tapered section is guaranteed. In this case, a significant enhancement in the pulse width and the peak power can be achieved.

Vary the QD layer number

Besides above methods, larger S value can be achieved alternatively by decrease the QD layer (QDL) number inside the device active region. Our colleagues Mesaritakis *et al.* from University of Athens (Greece) has found that although device with less QDLs are expected to show better ML performances, the early onset of ES lasing in these devices limits the maximum peak power and minimum pulse width that can be achieved. Our simulations fully confirmed their experiment findings and supplied proper theoretical interpretations of these results.

In this part, we consider three straight InAs/InGaAs QD lasers with total length of 2 mm, gain-to-absorber length ratio of 85:15, ridge width of 6 μm , high reflection coating at the SA side facet with $R_{0,k} = 99\%$ ($k = \text{ES, GS}$), low reflection coating at the output facet with $R_{L,k} = 10\%$, and different QDL numbers of 5, 10 and 15.

Two different theoretical approaches are used aiming to predict the variations of mode locking performance in these devices. The first approach is based on the assumption that mode-locking can be represented just by a simple net-gain modulation phasor with a time constant matching the characteristic round-trip time of the cavity [88]. Although this approach has been used successfully in the past in order to optimize the geometry of multi-section QD lasers, it does not take into consideration the gain dynamic imposed by the existence of two discrete energy levels (GS/ES). On the other hand, the experimental results proved that higher state dynamics and in particular the onset of ES lasing has a considerable effect on GS mode locking performances. Consequently, a second theoretical approach is utilized, i.e., the DDE numerical model which includes GS/ES carriers and photons dynamics. With this method, a detailed investigation of the 2 mm devices is performed and an explanation for the trends observed experimentally is therefore proposed. Model parameters used in the simulations are essentially those reported in Table 3.1. They correspond to the case of InAs/InGaAs Dots-in-a-Well lasers emitting around 1.3 μm and have shown good agreement between the simulations and the experiments [74].

The material gain at the ground state ($g_{0,GS}$) and excited state ($g_{0,ES}$) wavelength is computed as a function of the applied current density J for devices of different QDLs (Fig. 3.8). In order to achieve this, the steady state solutions of the rate equation system (see Section 2.2) for QD-based

Table 3.1: Passively mode-locked laser: main model parameters used in the rate equation system

Symbol	Description	Values
H_W	QW width	5 nm
η_0	Effective refractive index	3.3445
N_{lay}	number of QD layers	5
N_d	QD surface density	$2.7 \cdot 10^{10} \text{ cm}^{-2}$
$2\hbar\Gamma$	gain spectral bandwidth	34 meV
Γ_{xy}	field confinement factor	5.24%
$g_{0,k}$	material gain coefficient k = ES, GS	379.4, 227.6 cm^{-1}
$\tau_{QW \rightarrow ES_2}$	relaxation time from QW to ES ₂	0.3 ps
$\tau_{ES_2 \rightarrow ES_1}$	relaxation time from ES ₂ to ES	0.2 ps
$\tau_{ES_1 \rightarrow GS}$	relaxation time from ES to GS	0.2 ps
$\tau_{Aug,k}$	Auger recombination times from k = ES ₂ , ES, GS	110, 275, 660 ps
$\tau_{sp,k}$	spontaneous emission recombination times from k = ES ₂ , ES, GS	2, 2.7, 2.7 ns
$\tau_{nr,k}$	interband recombination times from k = SCH, WL	400, 400 ps
$\hbar\omega_k$	interband transition energies for k = ES ₂ , ES, GS	1.114, 1.054, 0.9879 eV
V_{bi}	built-in potential of the p-i-n junction	-0.8 V
α_i	intrinsic waveguide losses	2.1 cm^{-1}

medium have been computed assuming negligible optical power in the laser cavity. In Fig. 3.8, markers have been included in the computed gain curves indicating the GS/ES threshold gain $g_{th,GS/ES}$ for the two-section devices which are calculated according to the Eq. (3.9). For the investigations in this part, $\alpha_i = 2.1 \text{ cm}^{-1}$, $\alpha_{SA,GS} = 227 \text{ cm}^{-1}$ and $\alpha_{SA,ES} = 379 \text{ cm}^{-1}$.

As expected, the required GS threshold gain $g_{th,GS}$ decreases with increasing the QD layer number, due to higher field confinement factor ($\Gamma_{xy} = 0.0524, 0.083, 0.1056$ were calculated for the 5, 10 and 15 QDL devices, respectively). For the 5 QD layers device, at GS threshold current $J_{th,GS}$, $g_{0,ES}$ is appreciable larger than that of GS. In this case, ES threshold current $J_{th,ES}$ is slightly smaller than $J_{th,GS}$. On the contrary, $g_{0,ES}$ is still well below $g_{th,GS}$ at GS threshold current in the 10 and 15 QDL devices

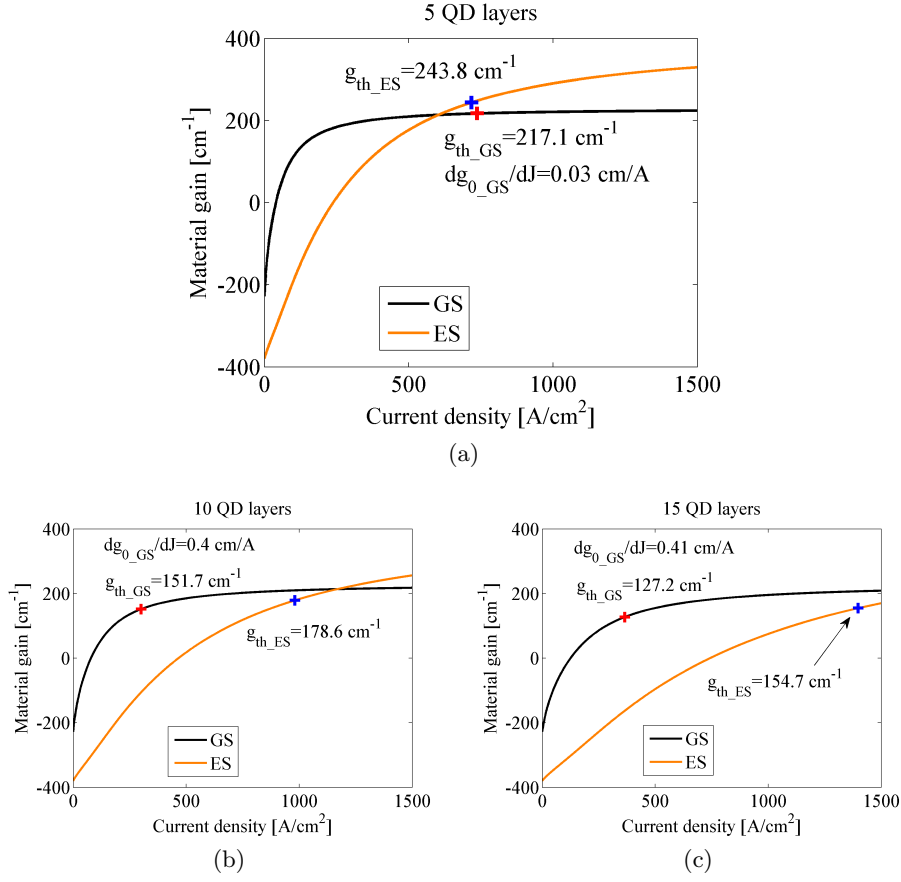


Figure 3.8: Dependence of GS (black) and ES (orange) material gain on the injection current density for devices with active region consisting of 5 (a), 10 (b), 15 (c) QD layers. Corresponding threshold gains (plus marker) and differential gains at GS/ES transitions are also indicated.

and therefore J_{th_ES} is much larger than J_{th_GS} . Furthermore, a decrease in the GS threshold gain leads to a significant increase in the differential gain dg_{0_GS}/dJ at J_{th_GS} when moving from 5 QDL case to 15 QDL one (Fig. 3.8).

Recently, an analytical expression [88] has been derived, aiming to evaluate the impact of different laser geometries on the efficiency of passive mode-locking. It has been obtained from the net-gain modulation phasor approach and has been successfully applied to predict functional QD laser geometries [88]. Its expression is:

$$\frac{\alpha_{SA_GS}}{g_{th_GS}} \frac{L_{SA}}{L_{gain}} > \left(\frac{(dg_{0_GS}/dJ)|_{g_{0_GS}=g_{th_GS}}}{(dg_{0_GS}/dJ)|_{g_{0_GS}=0}} \right)^2 = \left(\frac{1}{S} \right)^2 \quad (3.11)$$

where the right hand side term is reversely proportional to the square of the

well known stability parameter S (with respect to the standard definition of S parameter Eq. (3.4), linear relationship between dg_{0_GS}/dJ and dg_{0_GS}/dn is assumed in this approach, being n is the carrier density).

According to this inequality, both increasing α_{SA_GS}/g_{th_GS} and S will make Eq. (3.11) more easily to be satisfied and therefore benefit the ML operation (notice that L_{SA}/L_{gain} is constant for all devices).

For the devices under test, the parameter S decreases from 150 for the 5 QD layers laser, to 5.7 and 3.6 for the 10 and 15 QDL lasers, respectively. In addition, the ratio α_{SA_GS}/g_{th_GS} is 1.05 for 5 QDLs, while for 10 and 15 QDLs the ratio is increased to 1.5 and 1.77 respectively.

According to the above calculation, a significant deterioration of the ML stability and performances would be expected when increasing the number of QDL from 5 to 10, whereas similar performances should be achieved in devices with 10 and 15 QDL. These findings are qualitatively consistent with the experimental observations from Mesaritakis *et al.* only for the 10 and 15 QDL cases. The reason that the aforementioned simple analytical approach does not fully support the experimental findings in the 5 QDL case is based on the fact that this approach treats the mode locking procedure as a simple modulation of the GS net gain of the laser, without taking into consideration more complex dynamic effects present in QD materials. For example, it does not take into consideration the existence of discrete energy states (GS-ES), and the strong coupling of the free carriers between these two states.

Investigation that is more precise has been done using the DDE numerical model. The results are reported in Fig. 3.9 where ML maps, showing the pulse peak power and pulse width as a function of the injection current and the reverse bias voltage are shown. White regions correspond to CW operation; shaded areas show unstable GS ML due to: onset of ES lasing in the 5 QDL case and large amplitude fluctuations induced by the spontaneous emission noise in the 10 and 15 QDL cases.

In the 5 QDL devices, J_{th_ES} is slightly smaller than J_{th_GS} (Fig. 3.8a), ES lasing starts first when injection current increases from the threshold. However, this sole ES lasing regime is limited only to a very small current range just above the threshold (beyond the bias range shown in Fig. 3.9). Then at higher current, due to the competition between the pulse-induced depletions of the gain and absorption at GS/ES, sole GS lasing is preserved which inhibits simultaneous lasing from ES. However, considerably increasing the current and reverse voltage, aforesaid restriction in the ES lasing is appreciably reduced allowing the onset of the ES lasing (detailed investigation and explanation of this kind of behaviours will be reported in 3.5). Furthermore, we found that the simultaneous existence of ES lasing destabilizes the ML regime achieved at the GS wavelength and it therefore represents a limitation in the maximum achievable average and peak powers for sole GS ML in the 5 QDL devices.

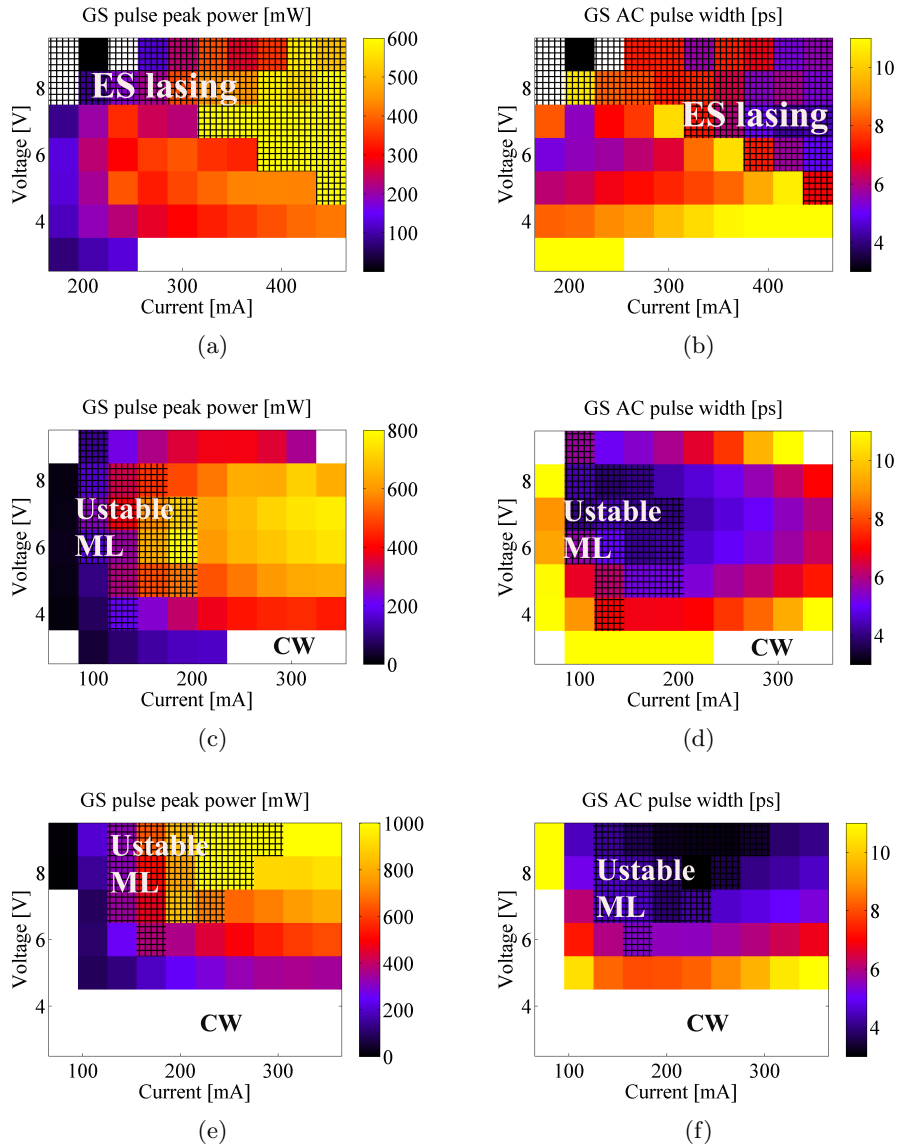


Figure 3.9: Maps of the pulse peak power and the pulse width with the same variation span of the injection current and the reverse bias voltage for 2 mm device with 5, 10, 15 QD layers. Shaded regions represent unstable ML performances, which is mainly induced by ES lasing for 5 QDL device, whereas by unbalanced gain and absorption dynamics for 10 and 15 QDL devices.

This is consistent with the experimental findings from Mesaritakis *et al.*, where the onset of the ES lasing was observed to limit the range of stable GS ML in the 5 QDL devices. On the contrary, in the 10 QD layers case, at GS threshold, ES gain remains far below its own threshold and therefore only mode locking from GS can be found over the whole investigated bias

range. This allows obtaining stable ML at larger current above threshold and therefore a significant improvement in the peak power as well as slightly shorter values of pulse width are achieved. Therefore, although above an analytic approach predicts better pulse characteristics in the 5 QDL devices, this advantage is completely counteracted by the ES lasing, which leads to a degradation of the GS pulses.

Finally, consistent with the slight reduction in the S parameter, moving from 10 QDL to 15 QDL, the region of stable ML decreases, whereas similar values of peak power and pulse width are obtained.

As a conclusion, ML performances in the 5 QDL device are limited by the early onset of the ES lasing while the 15 QDL device suffers limited stable ML range due to smaller S parameter, therefore the 10 QDL device exhibits relative better pulse performances.

3.3.2 Lasers with the same value of the stability parameter S

We have shown in previous subsection that device with larger S value generally would obtain pulse with shorter width and higher peak power. However, even for device with the same S value, it is still possible to enhance the ML system by properly changing the laser configuration. We show in this subsection the investigation of the performance optimization for the monolithic two-section passively mode-locked quantum dot lasers using the FDTW model changing simultaneously the length of the saturable absorber and the cavity reflectivity and keeping the S value. We demonstrate that, by properly choosing these two parameters, a reduction in the pulse width from 4.4 ps to 930 fs and an increase in the product of the peak power and the average power from 0.012 W^2 to 0.2 W^2 are obtained.

The simulations in this subsection have been performed using the FDTW model for 3 mm long InAs/InGaAs QD ML laser with 10 QD layers. We point out that the investigation presented in this subsection is quite general; therefore the conclusions drawn here can be also exploited in the design of lasers with different total length or different number of QD layers.

Five straight two-section FP lasers are considered; all have the same total length L of 3 mm, ridge width W of $6 \mu\text{m}$, high-reflection coating at the SA side facet with reflectivity R_0 of 95% and the same 10 QD layers active region, while the length of the SA L_{SA} and the reflectivity at the gain section side facet R_L are varied to obtain the same threshold material gain g_{th} for each device. The material-related parameters used in the rate-equation associated to the FDTW model are reported in Table 3.2.

In Fig. 3.10, the GS and ES material gains, as a function of the current density, are shown. As we pointed out in previous subsection, for straight monolithic QD lasers, higher S can be obtained when operating the gain section in a strong population inversion regime, equivalent to operate with a

Table 3.2: Straight index-guided mode-locked laser: main model parameters used in the rate equation system

Symbol	Description	Values
H_W	QW width	5 nm
η_0	Effective refractive index	3.3445
N_{lay}	number of QD layers	10
N_d	QD surface density	$2.7 \cdot 10^{10} \text{ cm}^{-2}$
$2\hbar\Gamma$	gain spectral bandwidth	34 meV
Γ_{xy}	field confinement factor	9.07%
$g_{0,k}$	material gain coefficient k = ES, GS	$331.2, 198.6 \text{ cm}^{-1}$
$\tau_{SCH \rightarrow QW}$	relaxation time from SCH to QW	24.6 ps
$\tau_{QW \rightarrow ES_2}$	relaxation time from QW to ES ₂	0.3 ps
$\tau_{ES_2 \rightarrow ES_1}$	relaxation time from ES ₂ to ES	0.2 ps
$\tau_{ES_1 \rightarrow GS}$	relaxation time from ES to GS	0.2 ps
$\tau_{Aug,k}$	Auger recombination times from k = ES ₂ , ES, GS	110, 275, 660 ps
$\tau_{sp,k}$	spontaneous emission recombination times from k = ES ₂ , ES, GS	2, 2.7, 2.7 ns
$\tau_{nr,k}$	interband recombination times from k = SCH, WL	300, 300 ps
$\hbar\omega_k$	interband transition energies for k = ES ₂ , ES, GS	1.114, 1.054, 0.9879 eV
V_{bi}	built-in potential of the p-i-n junction	-0.8 V
β_{sp}	spontaneous emission coupling factor	10^{-4}
α_i	intrinsic waveguide losses	3 cm^{-1}

g_{th} close to saturation. But if g_{th} is too close to the GS and ES gain-crossing condition, there maybe a risk of ES lasing due to restricted fabrication tolerance and a risk of instability induced from the too high carrier population in the ES. According to these considerations, g_{th} has been chosen in this case as 175 cm^{-1} (see the square marker in Fig. 3.10) and kept the same for all the considered devices.

The corresponding values of L_{SA} and R_L for the considered devices have been estimated using Eq. (3.9). In this case, $\Gamma_{xy} = 9 \%$ is the field con-

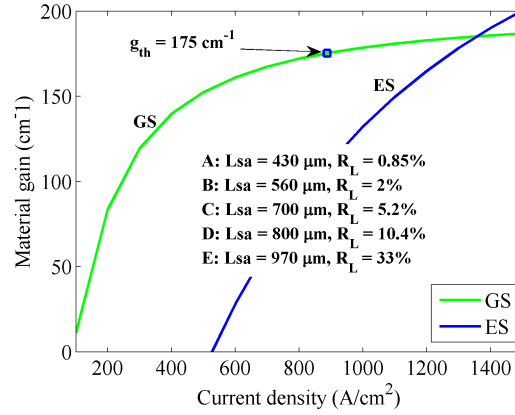


Figure 3.10: QD material gain from GS (green) and ES (blue) transitions as a function of the injection current density. The square marker represents the fixed threshold gain for the devices considered in the simulations. The corresponding SA length and the output power reflectivity are also shown.

finement factor within the 10 QD layers, $\alpha_{SA} = 198.6 \text{ cm}^{-1}$ is the QD unsaturated material absorption at GS transition and $\alpha_i = 3 \text{ cm}^{-1}$ is the intrinsic waveguide losses. The results of L_{SA} and R_L for the five considered devices (A-E) are reported in Fig. 3.10. Following the above procedure we ensure that every device operates at almost the same S parameter at threshold.

In addition to the usual measured pulse parameters, a figure-of-merit (FOM) [92], i.e., the product of the average power and the peak power ($P_{avg} * P_{peak}$), has been used as an indicator for device comparison. The ML laser pulse average power, peak power, deconvoluted autocorrelation pulse width and FOM for the devices (A-E in Fig. 3.10) are reported in Fig. 3.11, as a function of the injection current and at constant SA reverse voltage of -5 V.

All devices have been simulated in a current range of 200 mA starting from 20 mA above the corresponding threshold current I_{th} . The results, only for the bias conditions achieving stable ML, are plotted in Fig. 3.11. The first conclusion from this figure could be that the configurations with larger L_{SA} exhibit an increased range of bias conditions achieving stable ML. Since S has a constant value for all the considered devices, these results demonstrate that changing L_{SA} allows improving in the stability of the ML laser. Furthermore these numerical results also confirm a previous theoretical statement that lasers with smaller cavity loss ($\alpha_i + \alpha_m$) are more likely to show stable ML without self-pulsing envelope [88], [93].

For all devices the increase of the injection current results in an increase in the pulse width (Fig. 3.11c). Additionally, devices with longer SA and higher output reflectivity exhibit a monotonic reduction in the shortest pulse

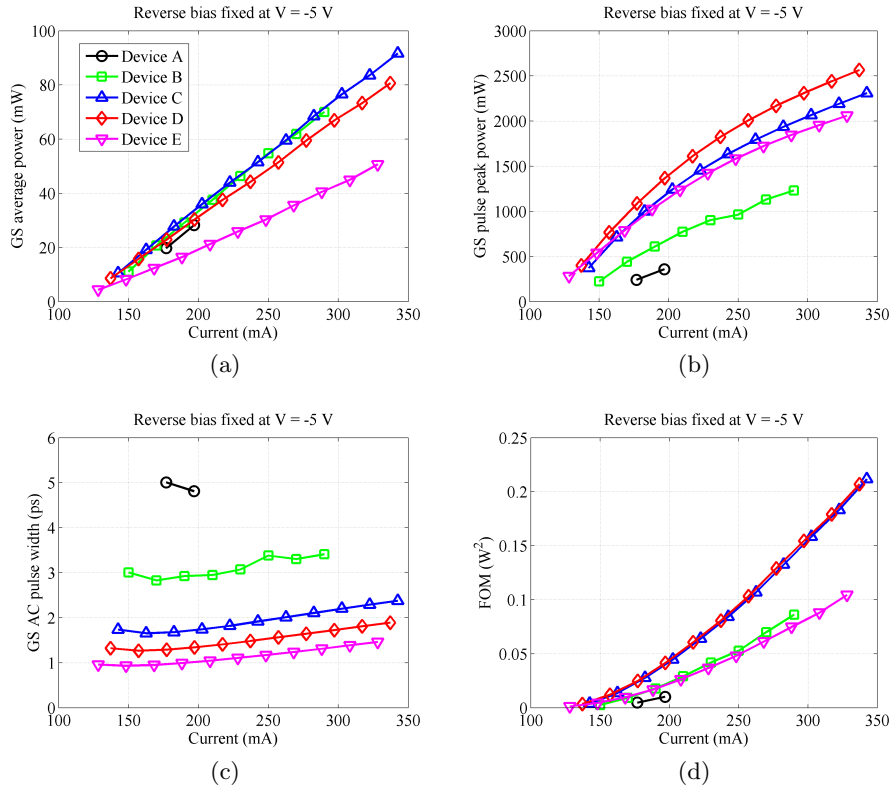


Figure 3.11: Average power (a), peak power (b), deconvoluted autocorrelation (AC) pulse width (c) and FOM (d) at the fixed reverse-bias voltage $V = -5$ V and as a function of the injection current for devices A (square), B (circle), C (upward-pointing triangle), D (diamond) and E (downward-pointing triangle) in Fig. 3.10.

width from 4.4 ps to 930 fs.

This behaviour has also been observed in [74], [89], where only L_{SA} has been increased. In [74], it was proposed that the pulse shortening in devices with longer SA is due to the significant increase in the gain saturation energy (so larger S) associated to a total-carrier-density depletion mechanism and consequently to a stronger spectral hole burning (SHB). The pulse width is therefore reduced due to the ultrafast SHB carrier dynamics. In our case with fixed S , above mechanisms and the influence induced by them do not change from device to device. Under this condition, we still observe shorter pulse in device with longer SA. This result can be explained as follows. The S parameter and the analytical definition for the gain/absorption saturation energy are related only with the cross-section geometry of the device and do not take into account the longitudinal saturation effects in the cavity. But the formation of a pulse is a cumulative process taking place along the cavity and therefore the non-uniform longitudinal saturation effects along

the SA and gain sections are also determining for the reduction of the pulse width.

Different behaviour can be observed in other figures. In Fig. 3.11a, the light-current (LI) characteristics show similar slope when moving from device A to C. While further increasing the reflectivity (device D and E) will lead to a decrease in the slope of the LI characteristic. In Fig. 3.11b, the achieved peak power increases continuously from device A to C due to the reduction in the pulse width. Then, since the reduction in the pulse width exceeds the decrease in the average power, device D exhibits higher peak power with respect to device C. Opposite behaviour happens in device E. By combining the results in Fig. 3.11a and 3.11b, it can be seen from Fig. 3.11d that the optimum configuration which has the highest FOM (0.2 W^2 in the considered bias range) should have a L_{SA} between 700 and 800 μm and a R_L between 5% and 10%.

Very similar trends are also observed at other reverse-bias voltages, except at lower reverse-bias where configurations with smaller L_{SA} may not achieve stable ML at all.

We demonstrate in this subsection that instead of the typically used low value of the output reflectivity (5% to 1%) [74], [94], an appropriate higher value of it with a proper length of the SA allows to obtain more stable ML, shorter pulses and higher FOM.

3.4 Relation between the intracavity pulse evolution and the ML performances

Quantum dot based two-section passively mode locked semiconductor lasers have been intensely investigated in the last ten years in order to achieve better ML properties. Various methods, such as increasing the absorber/gain length ratio [89], introducing a passive section [95], using novel scheme like tapered gain section [96], have been proposed and the experimental results have demonstrated high quality pulses with pulse width in the sub-picosecond range and peak power in the Watt range.

Full understanding of the dynamics governing the pulse formation in the ML lasers is always crucial to promote new design ideas for the device performance improvement. Therefore, theoretical investigations are essential to support the experimental investigations. To this end, both analytic theories and the numerical simulations of the QD-based ML lasers have been exploited. Although simpler, analytic equations are less reliable when applied to study the detailed dynamics in the QD devices [53], [88]. On the contrary, rigorous numerical models with acceptable computational cost have achieved increasing importance in the last years [54].

In previous section, we presented many methods to achieve better ML performances. In order to get further insight of the complex ML systems,

in this section, we study the influence of the intracavity pulse evolution on the pulse properties. The FDTW model shown in Section 2.4 has been used in this analysis. Starting from the most commonly used laser configuration, we investigated systematically the possibility to optimize the performances of a passively ML QD laser by varying the SA length, the total cavity length and the facet reflectivities. According to the simulation results, we found that changes in the laser configuration lead to consequent changes in the intracavity pulse energy (PE) evolution and the gain/absorption distribution which then contribute to the device performance variations. Particularly, it has been always observed that, at the same effective pumping level, the higher the PE impinging the SA, the smaller the pulse width.

In Subsection 3.4.1, a brief description of the investigation approach and the considered devices is presented; main discussion of the influence of the device parameters on the intracavity PE evolution and the pulse properties is shown in Subsection 3.4.2.

3.4.1 Investigation approach and the considered devices

Using the single-population FDTW model, the evolution of the optical field when propagating in forward ($+z$) and backward ($-z$) longitudinal directions within the device cavity and the carrier dynamics in the QD medium can be evaluated. The material related model parameters are given in Table 3.2.

Our study starts from a laser (device A) with the most commonly used configuration in the literature for high power short pulse generation [11], [89]. In this device the total length L is 2 mm, the ridge width W is $6 \mu\text{m}$, the SA length L_{SA} is $287 \mu\text{m}$, the SA side facet is high-reflection (HR) coated with reflectivity R_0 of 95%, the low-reflection (LR) coated facet has reflectivity R_L of 4.2% and the active region consists of 10 stacks of InAs/In_{0.15}Ga_{0.85}As Dots-in-a-Well layers. Schematic of this laser is given in Fig. 3.12a. In the following subsection, most of these parameters will be modified and the corresponding influences on the device performances will be shown.

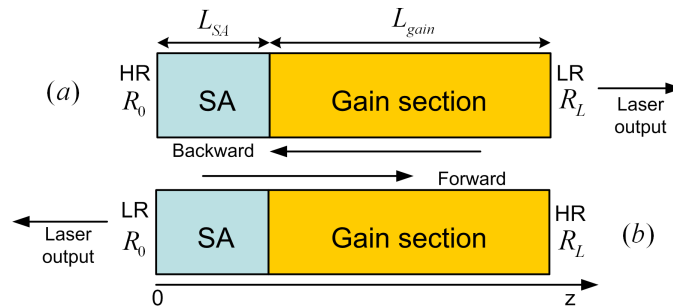


Figure 3.12: Schematic of the two-section ML laser with output from the gain section side facet (a) and the configuration with output from the SA side facet (b).

To compare different devices, the following conditions are obeyed throughout this work so that each device has almost the same operation condition.

- 1 All the devices operate at the same S value. As pointed out previously, for the straight monolithic QD laser, the same gain saturation energy can be achieved by fixing the threshold gain g_{th} , since in this way the differential gain which determines the gain saturation energy is fixed. We have chosen $g_{th} = 175 \text{ cm}^{-1}$ for all the considered devices, since it is neither too low to achieve enough S nor too high to avoid ES induced instability (competition between the GS and ES emissions will be shown in Section 3.5).
- 2 Since the optical power is negligible below the laser threshold, the effective part of the injected current for pulse energy increasing in the laser cavity is the part above the threshold current I_{th} . We call therefore this part of current as the effective pumping current ($I_{eff} = I - I_{th}$) and this parameter unless otherwise specified is fixed at 40 mA.
- 3 To achieve the same absorption saturation energy and absorption recovery rate, the reverse bias voltage of the SA is always set to -5V. Another reason for this high reverse voltage is to avoid the trailing edge instability in the ML which is always observed in the device with high S value [74].

In order to satisfy the condition 1, g_{th} is fixed, and the corresponding structural parameters are estimated using Eq. (3.9). In this case, the field confinement factor $\Gamma_{xy} = 9 \%$, the QD unsaturated material absorption at GS transition $\alpha_{SA} = 198.6 \text{ cm}^{-1}$ and the intrinsic waveguide losses $\alpha_i = 3 \text{ cm}^{-1}$.

3.4.2 Investigation and discussion

Let study first the device A. Fig. 3.13(a) shows the spatio-temporal evolution of the optical power of a GS pulse oscillating inside the laser cavity. The ordinate axis indicates the location along the total cavity length with the SA side facet at $z = 0$ and the gain section side facet at $z = L$ (see also Fig. 3.12). This map highlights the spatially dependent coupling between the forward (F_f) and backward (F_b) travelling optical fields. As shown in Fig. 3.13b/c, the field absorption/gain dynamics are highly dependent on the considered section z , since the relative delay between the times when F_f and F_b crosses that section varies with z . At cut 1 (Fig. 3.13b), this delay is quite short, therefore the backward field-induced absorption saturation recovers only slightly when the forward field peak arrives. Whereas at cut 2 (Fig. 3.13c), the delay is longer and allows the gain saturation to recover